

## Supplementary Materials for

### Structure of Arp2/3 complex at a branched actin filament junction resolved by single-particle cryo-EM

Bojian Ding<sup>a†</sup>, Heidy Y. Narvaez-Ortiz<sup>b†</sup>, Yuvraj Singh<sup>c</sup>, Glen M. Hocky<sup>c</sup>, Saikat Chowdhury<sup>a,d,e\*</sup>, and Brad J. Nolen<sup>b\*</sup>

<sup>a</sup> Department of Biochemistry and Cell Biology, Stony Brook University, Stony Brook, New York, USA

<sup>b</sup> Department of Chemistry and Biochemistry and Institute of Molecular Biology, University of Oregon, Eugene, Oregon, USA

<sup>c</sup> Department of Chemistry, New York University, New York, New York, USA

<sup>d</sup> CSIR-Centre for Cellular and Molecular Biology, Hyderabad, India

<sup>e</sup> Academy of Scientific and Innovative Research (AcSIR), India

†These authors contributed equally.

\*Corresponding authors: Saikat Chowdhury, Brad J. Nolen

**Email:** saikat@csirccmb.org, bnolen@uoregon.edu

#### **This PDF file includes:**

- Supplemental Information
- Supplementary Figures 1 to 20
- Supplementary Tables 1 and 2
- Supplementary Movie Legends
- Supplementary Methods

## Supplemental information

### Phalloidin binds the mother and daughter actin filaments and Arp2/3 complex

Phalloidin binds to the inner face of the two actin protofilaments, interacting with three consecutive subunits and burying a total of  $\sim 550\text{-}600 \text{ \AA}^2$  (Fig. S5). In addition to binding at the interface of actin subunits or actin and Arp2, one molecule of phalloidin binds at the interface of actin D1, Arp2 and Arp3 (Fig. S5). This bound phalloidin may help stabilize the filament-like arrangement of Arp2 and Arp3, potentially explaining a previous report showing that phalloidin binding increases WASP-mediated activation of the complex (1).

We wondered if phalloidin might influence the interactions of Arp2/3 complex with mother filaments of actin. Previous studies showed that under some conditions phalloidin influences the conformation of the actin D-loop, a flexible loop in subdomain 2 that can respond to the nucleotide binding state of actin (2–5). Examination of the branch junction structure shows that Arp2/3 complex contacts the D-loop of mother filament actin subunit M2 (Fig. S5C), suggesting phalloidin might influence mother filament binding. However, structural superpositions showed that the mother filament from the branch junction structure is nearly identical to phalloidin-free ADP-bound actin filaments, in which the actin D-loops adopt a “closed” conformation (Fig. S6B) (2, 4). This result is consistent with previous observations showing that phalloidin has little or no effect on the conformation of aged (ADP-bound) actin filaments (note that the branched junctions visualized here were aged before adding phalloidin) (6). In addition, mutational analyses showed the interaction between Arp3 and the actin M2 D-loop does not contribute favorably to the interaction between Arp2/3 complex and actin filaments (7). Therefore, we do not expect phalloidin significantly influences the contacts of Arp2/3 complex with ADP-bound mother filaments. Whether the contacts of Arp2/3 complex with ATP- or ADP-Pi-loaded actin filaments are distinct, and whether the interactions could be influenced by phalloidin is an important open question.

The rationale outlined above also argues against a significant influence of phalloidin on the contacts between Arp2/3 complex and the pointed end of the daughter filament. While the D-loops of actin subunits D1 and D2 insert into the barbed ends of Arp2 and Arp3 (Fig. 3), they adopt the closed conformation observed in both phalloidin-

bound and phalloidin free ADP-bound actin filament structures (Fig. 3B,C, S6B) (2, 4, 6). Nevertheless, future studies aimed at solving the branch junction structure in the absence of phalloidin and in different nucleotide binding states will likely provide important new insights.

### **Interactions between the D-loop of Arp2 and ARPC3 are important for Arp2/3 activation**

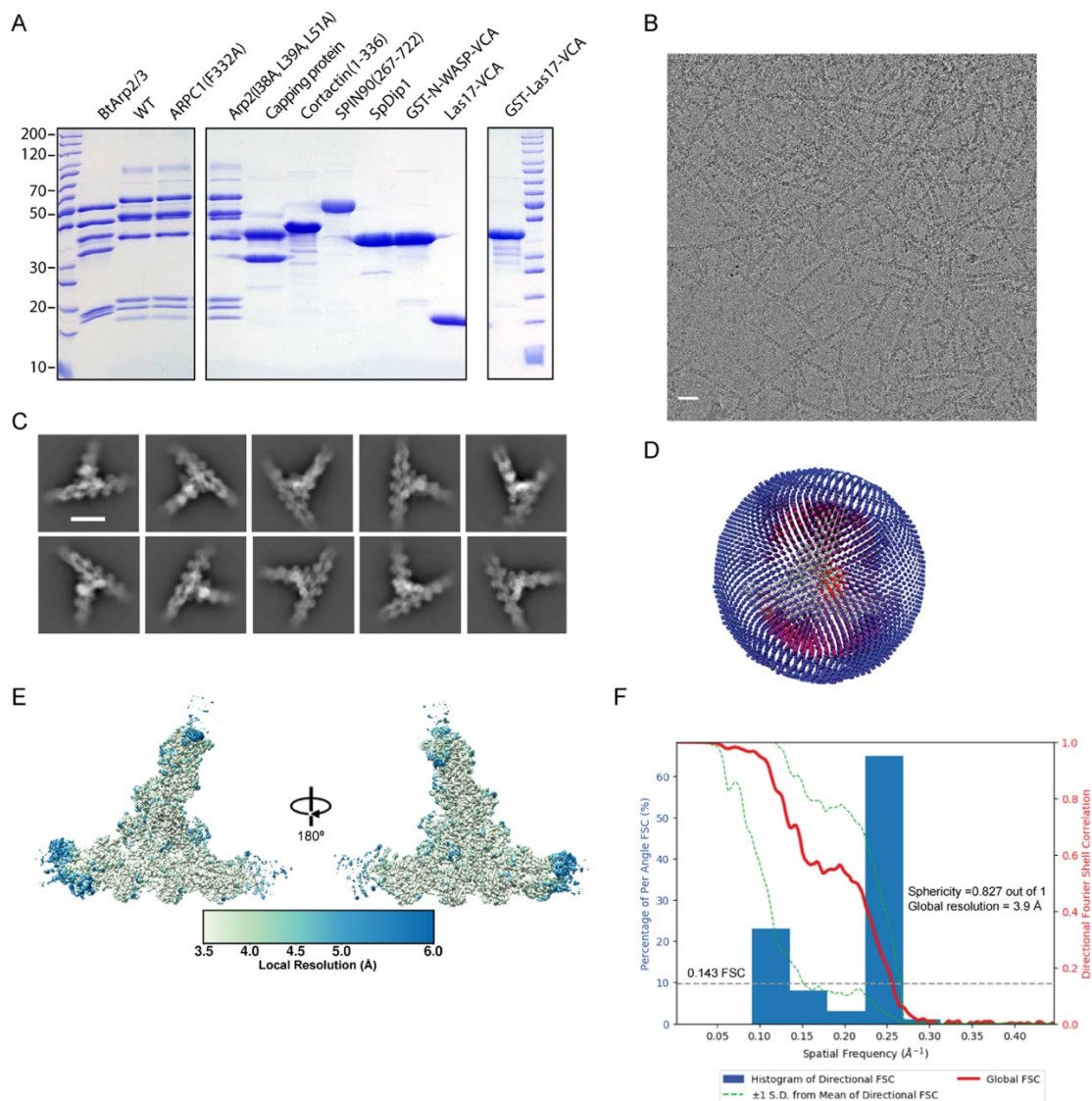
To better understand the conformational changes that lead to activation we examined how the intra-subunit contacts in Arp2/3 complex change during activation. An analysis of buried surface area between subunits showed one striking difference between the active and inactive states: Arp2 contacts ARPC3 in the active state, burying  $\sim 700 \text{ \AA}^2$ , whereas it does not contact ARPC3 in the inactive state (Fig. S16). This interaction, first noted in the  $9 \text{ \AA}$  branch reconstruction (33), occurs because subunit flattening of Arp3 and movement of the Arps into the short pitch conformation bring the D-loop, a loop within Arp2 subdomain 2 that is disordered in inactive structures, into position to pack against a hydrophobic surface on ARPC3 (Fig. S17A,B). The Arp2 D-loop contributes residues Pro39, Ile40, Ile41, Val47, Ile52 to this interaction, with residues Ile60, Ile69, Pro112, Ile116 and Met169 forming the complimentary hydrophobic interface on ARPC3 (Fig. S17B). This interaction is clearly visible in our branched-junction structure but was not resolved in the Dip1-activated Arp2/3 complex structure, in which the D-loop of Arp2 is disordered (15). A triple mutation of three D-loop residues at the interface (Arp2(I38A, L39A, L51A)) significantly decreased the ability of Las17 to activate budding yeast Arp2/3 complex in pyrene actin polymerization assays, reducing the maximum polymerization rate in reactions containing  $1 \text{ \mu M}$  Las17 by  $\sim 72\%$  (Fig. S17C,D). This observation is consistent with a role for the Arp2 D-loop/ARPC3 interaction in stabilizing the active conformation. To determine if this interaction plays a general role in stabilizing the activated state we asked whether or not the triple mutant influenced Dip1-mediated Arp2/3 complex activation. The triple mutant decreased the ability of the Dip1 to activate budding yeast complex in pyrene actin polymerization assays, reducing the maximum polymerization rate in reactions containing  $5 \text{ \mu M}$  Dip1 by  $\sim 50 \%$  (Fig. S17E). Therefore, while the interaction between the D-loop of Arp2 and ARPC3 likely plays a role in stabilizing the active conformation of Arp2/3 regardless of the activating NPF, the interaction appears to be more important during WASP-mediated activation.

To determine if the interaction between the Arp2 D-loop and ARPC3 is important in cells, we monitored the dynamics of mNNG-Las17 and Abp1-TagRFP-T in a Arp2 D-loop deletion strain. The D-loop deletion strain showed a decreased accumulation of Abp1 at endocytic sites compared to the wild type, indicating the Arp2 D-loop is important for endocytic actin assembly (Fig. S17F-H). The mutation also decreased the percentage of endocytic actin puncta that moved off of the cortex and into the cytoplasm, suggesting defective internalization of endocytic cargo (Fig. S17I).

### **The conformation of the ARPC5 N-terminus is identical in inactive versus activated structures**

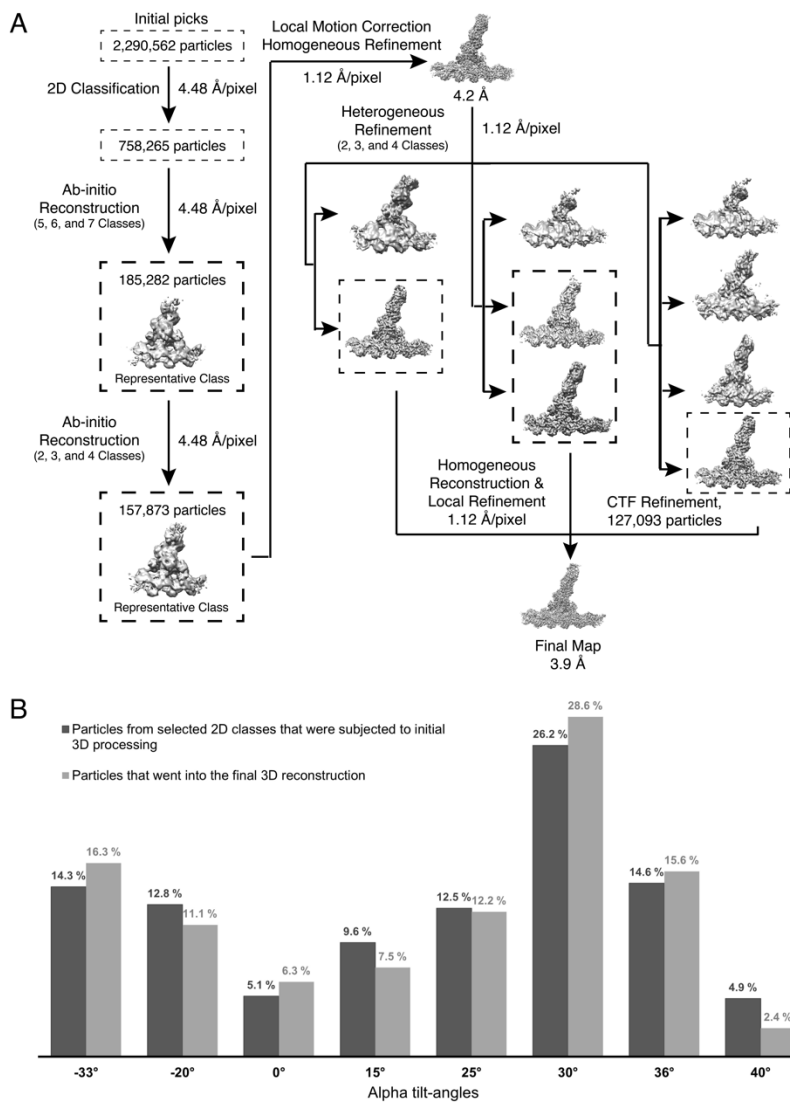
Within inactive Arp2/3 complex structures, the N-terminus of the smallest Arp2/3 complex subunit, ARPC5, stretches across the surface of ARPC1 and inserts between subdomains 3 and 4 in Arp2 (Fig. S18A). Previous biochemical and genetic data suggested that this interaction is important for stabilizing the attachment of Arp2 to the complex (8). However, the recent 9 Å cryo-EM branch junction reconstruction suggested a possible new function (9). In the 9 Å structure, there is no density for the ARPC5 N-terminus between subdomains 3 and 4 in Arp2 (9). Instead, unfilled electron density near the seam between ARPC1 and Arp2 was interpreted as a new potential binding site for the ARPC5 N-terminus. It was speculated that this new site might be engaged after activation and could stabilize the active state (9). Precisely how the proposed alternate conformation could specifically stabilize the activated state is unclear, because ARPC1 and Arp2 move as a rigid block during activation (Fig. 4, Movie S1). Nonetheless, we examined the 3.9 Å branch junction map presented here and found that the ARPC5 N-terminus shows clear and mostly continuous electron density, with only a small gap near the junction of the insert with the globular portion of ARPC5 (Fig. S18C-D). Importantly, it adopts the same conformation at the branch junction as it does in inactive Arp2/3 complex structures and in Dip1-activated Arp2/3 complex (Fig. S18B-D), bound between subdomains 3 and 4 of Arp2. Therefore, the current structure does not corroborate the existence of an alternative conformation for the ARPC5 N-terminus in the activated state.

### **Supplementary figures**



**Figure S1. Solution of cryo-EM structure of the branch actin filament junction. (A)** Coomassie-stained SDS-PAGE gel of proteins used for branch formation on EM grids and biochemical experiments. **(B)** A representative cryo-EM micrograph of branched actin network. Scale bar: 25 nm. **(C)** Representative 2D class averages of the branched actin junction. Scale bar: 25 nm. **(D)** Angular distribution plot showing the Euler angle distribution of the particles in the final 3D reconstruction. The height of each cylinder

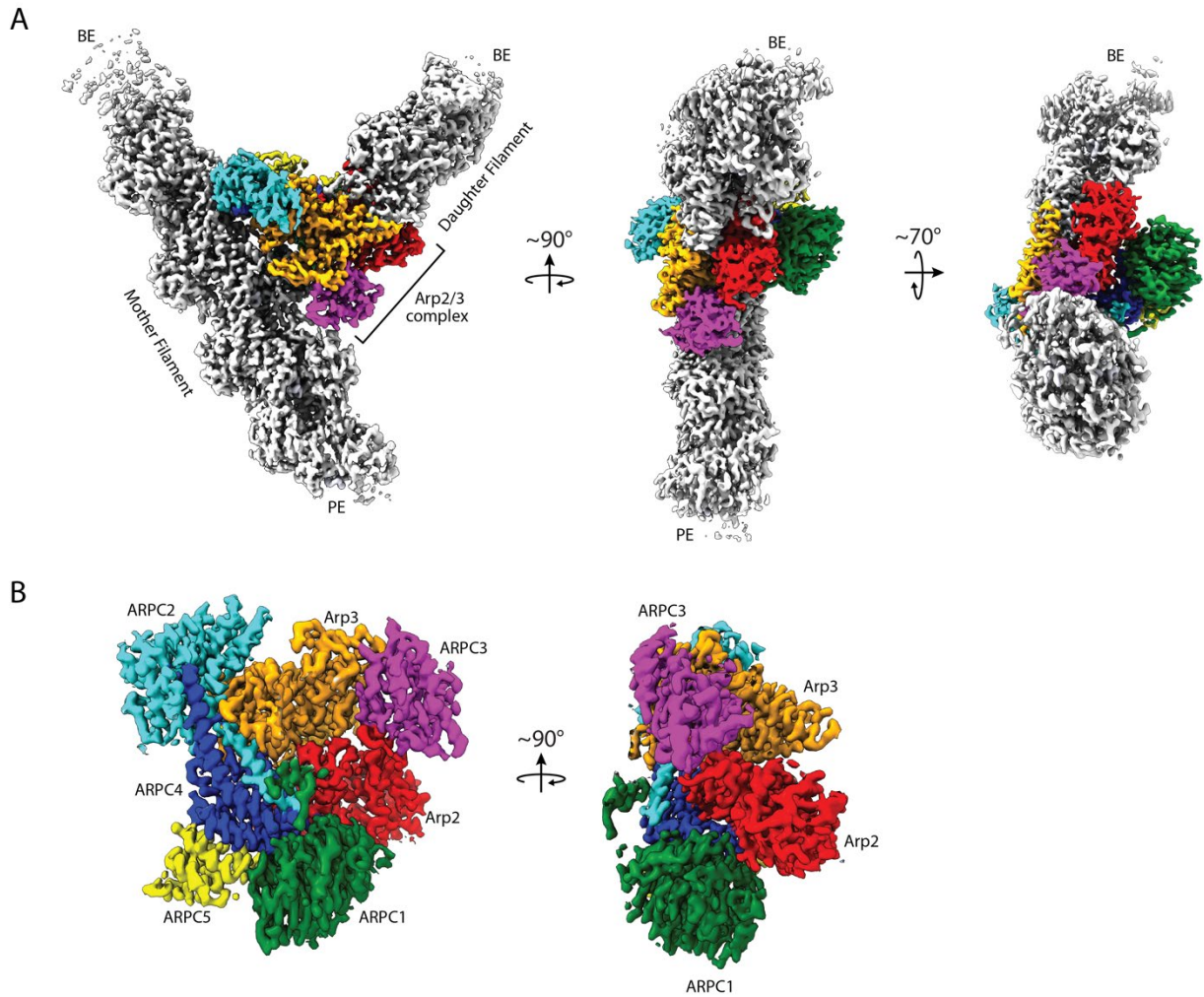
corresponds to the number of particles in each angular orientation. **(E)** The final cryo-EM reconstructed map of branched actin junction colored based on local resolution values. The majority of the reconstructed map was resolved between 3.5 Å and 4.2 Å with peripheral flexible actin subunits resolved to 6 Å. **(F)** Directional Fourier Shell Correlation (FSC) plot representing 3D resolution anisotropy in the reconstructed map. Blue histograms represent the percentage of directional resolution over the spatial frequency; the red line plot depicts the global FSC; the green dashed lines correspond to  $\pm 1$  standard deviation from mean of directional resolutions; and the grey dashed horizontal line indicates FSC of 0.143.



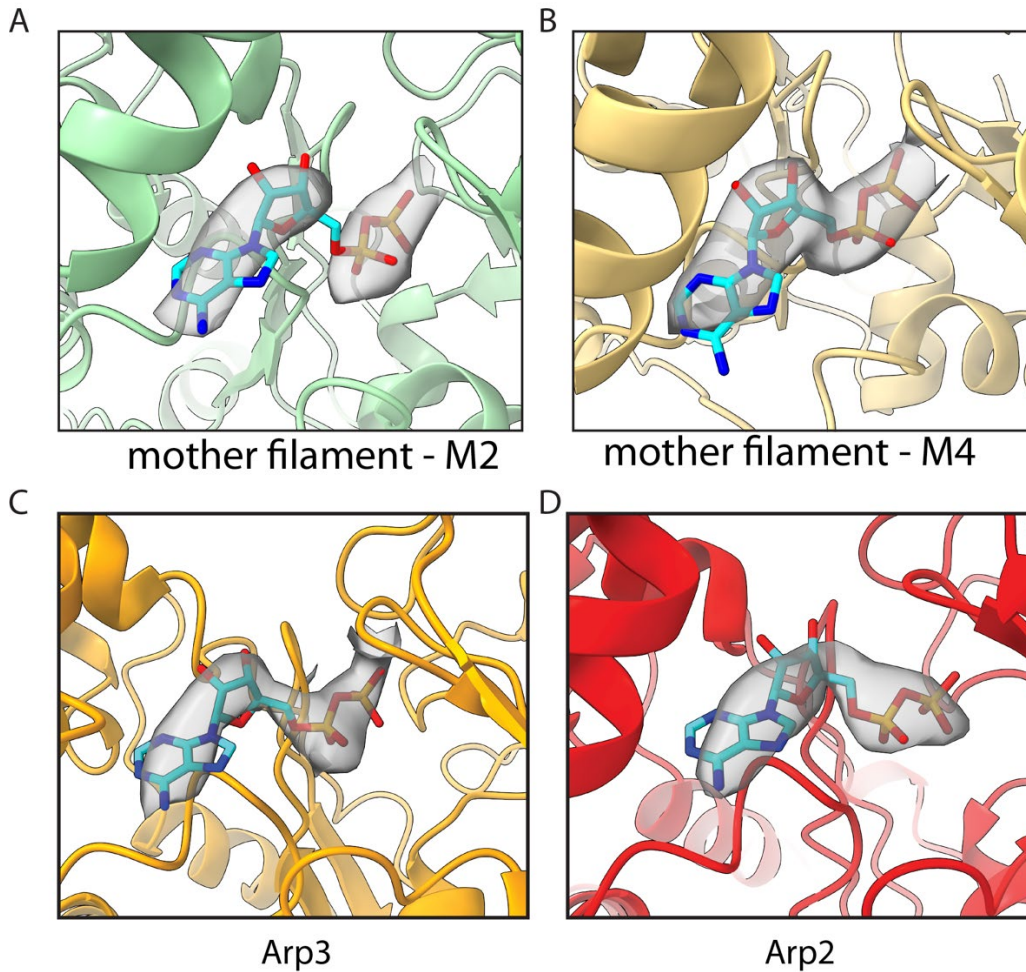
**Figure S2. Workflow for 3D reconstruction of branch junction. (A)** Overall single-particle data processing workflow of the branched actin junction cryo-EM dataset. Template picking with the 2D classes of branched junction, generated from initial reference-free Gaussian picked particles, lead to a stack of ~2.3 million particles. After discarding junk particles using iterative 2D classification the remaining particles were further classified through multi-class *ab-initio* reconstructions. Particles from the best resolved *ab-initio* classes were subjected to local motion correction followed by homogeneous refinement. This yielded a 4.2 Å reconstruction. Further heterogenous refinements with two, three, and four classes helped sort out 3D heterogeneity, and particles from the well-resolved branch junction 3D classes were combined and used for homogeneous refinement. CTF refinement and local refinement further improved the

resolution of final reconstruction to 3.9 Å. **(B)** Histogram showing percentage of particles from micrographs collected at each alpha-tilt angles that constituted the stack of particles from selected 2D classes prior to 3D processing (dark gray), and percentage of particles that went into the final 3D reconstructed map (light gray).

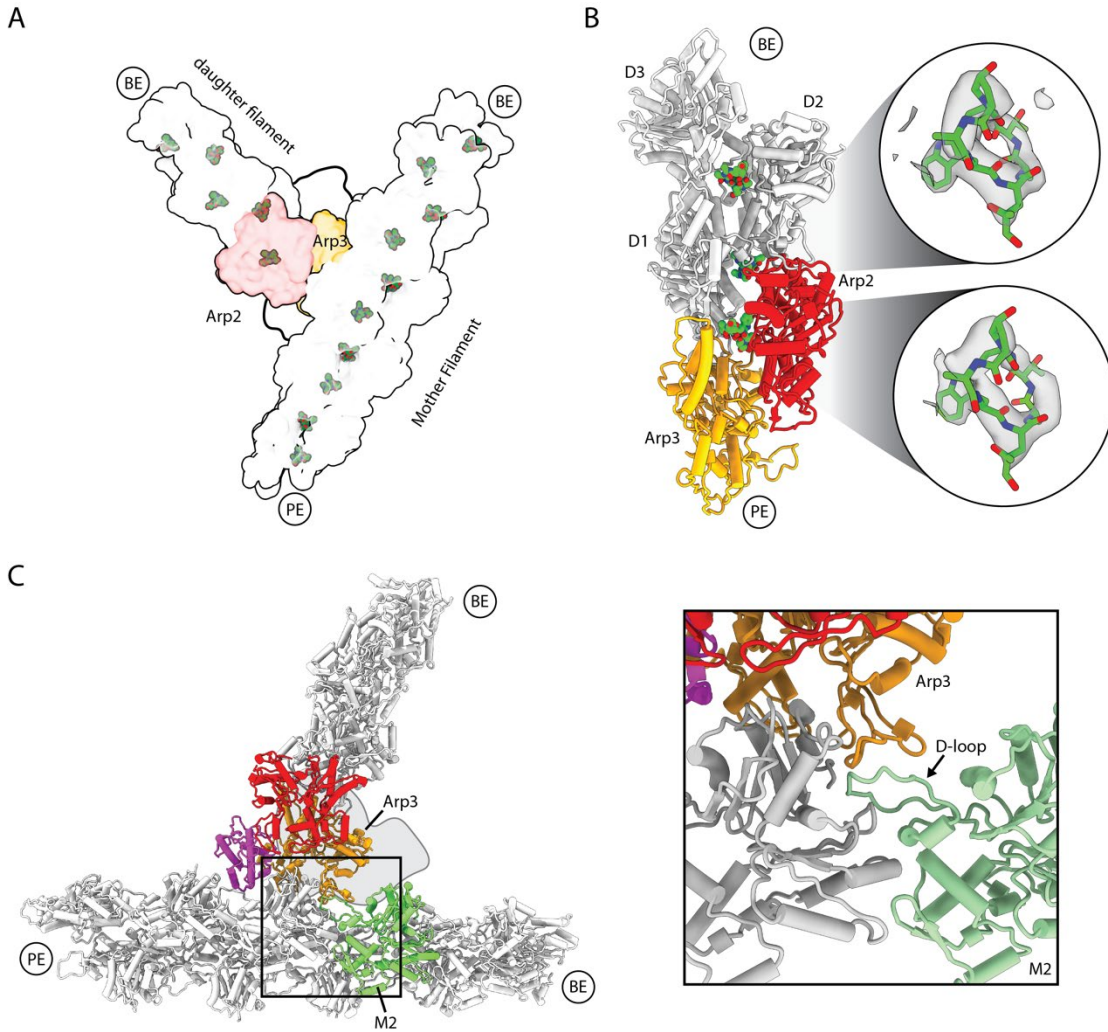




**Figure S3: Multiple views of branch junction and Arp2/3 complex density.** (A) Multiple views of branch junction density, with color coding identical to Figure 1A. (B) Multiple views of density of Arp2/3 complex at the branch junction, with color coding identical to Figure 1C.



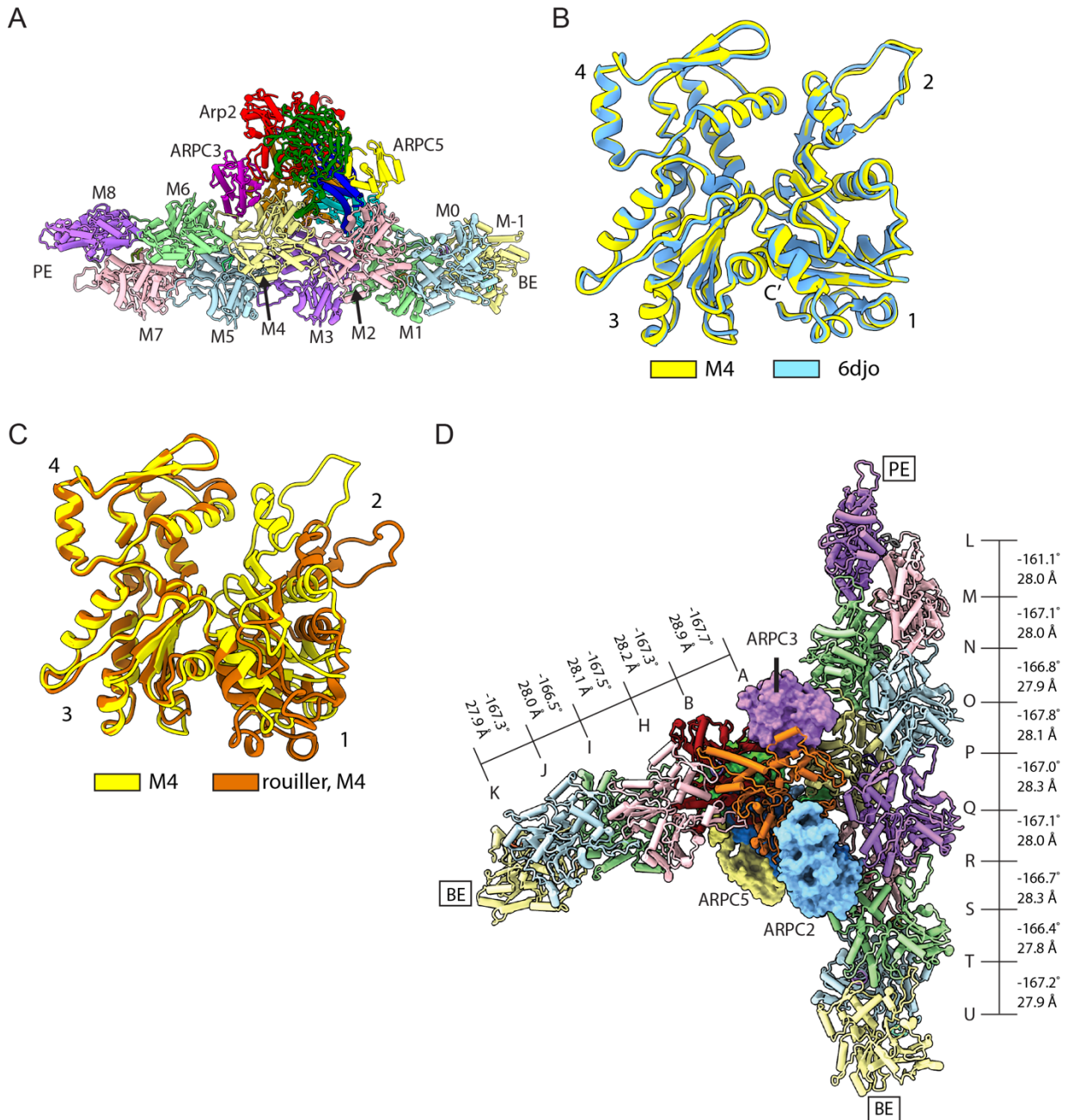
**Figure S4. Density consistent with ADP is present in the nucleotide binding clefts of actin subunits, Arp2, and Arp3 in the branch junction model.** Reconstructed density in the nucleotide binding clefts of actin subunit M2 (A), M4 (B), Arp3 (C) and Arp2 (D), is shown in transparent grey surface representation. Map surfaces within 2.4 Å of atoms in modeled ADP are shown.



**Figure S5. Phalloidin binds both the mother and daughter filaments. (A)** Transparent surface rendering of branch junction showing bound phalloidin molecules (green ball and sticks). Subunits of Arp2/3 complex other than Arp2 and Arp3 are omitted from surface rendering and are instead outlined with a black line. BE: barbed end, PE: pointed end. **(B)** Ribbon representation of Arp2, Arp3 and three actin subunits in the daughter filament showing bound phalloidin (green sticks). Density for phalloidin at the actin-actin-Arp2 and actin-Arp2-Arp3 interfaces is shown to the right. Only density within 3 Å of phalloidin is shown. **(C)** Ribbon representation showing branch junction and highlighting actin subunit M2 in the mother filament (green). ARPC1, ARPC2, ARPC4, and ARPC5 are depicted as

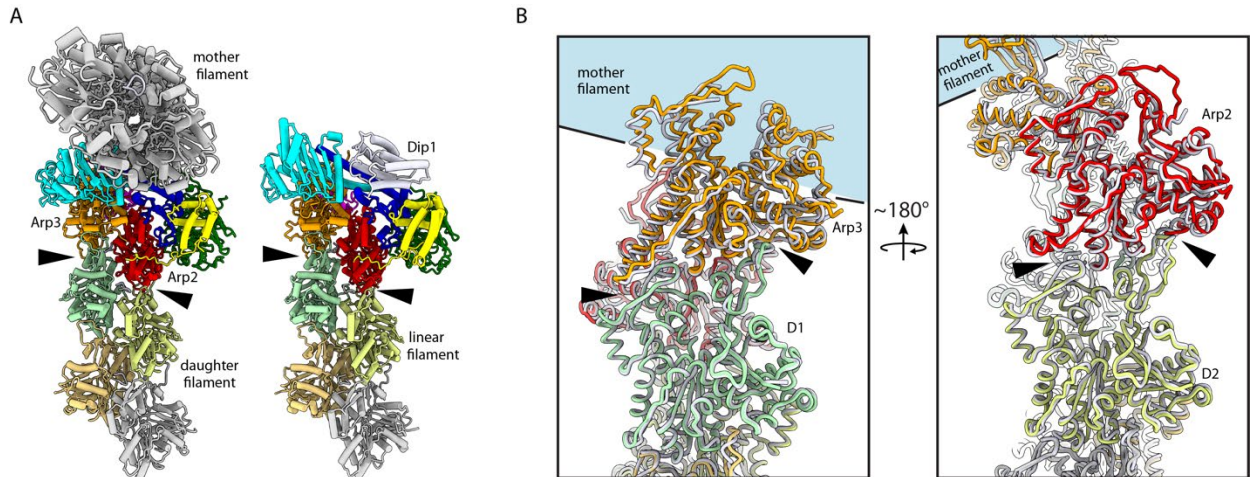
grey shape rather than ribbons to clearly show the interaction between Arp3 and the mother filament. Box indicates area shown in zoomed in view on the right.



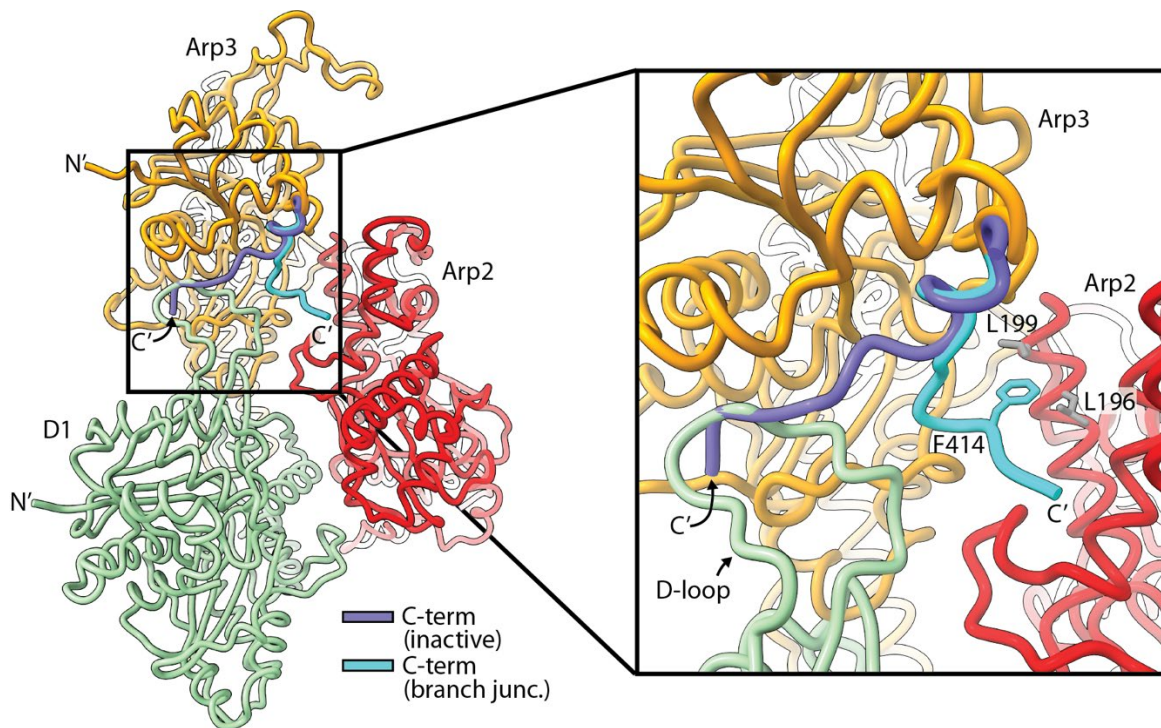


**Figure S6. Actin subunits within the mother filament have conformations nearly identical to high resolution cryo-EM structures of unbound actin filaments. (A)** Branch junction model presented here showing Arp2/3 complex bound to the site of a mother filament. Subunit M4 is distorted in the Rouiller, *et al.* structure (10). **(B)** Structural superposition of C $\alpha$  atoms from actin subunit M4 from the mother filament with an actin

subunit from the cryo-EM structure of ADP-bound actin filaments (PDB ID code 6DJO). **(C)** Structural superposition of C $\alpha$  atoms from subdomains 3 and 4 of actin subunit M4 from the mother filament with the equivalent actin subunit from the mother filament in the 26 Å reconstruction of a branch junction (10). **(D)** Branch junction model showing rise and twist between actin and actin-related subunits. BE: Barbed end, PE: pointed end.



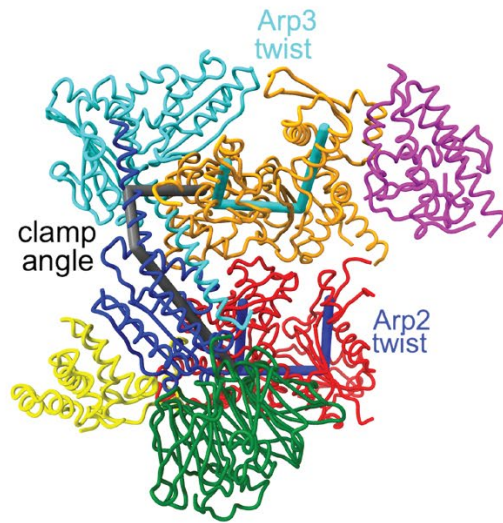
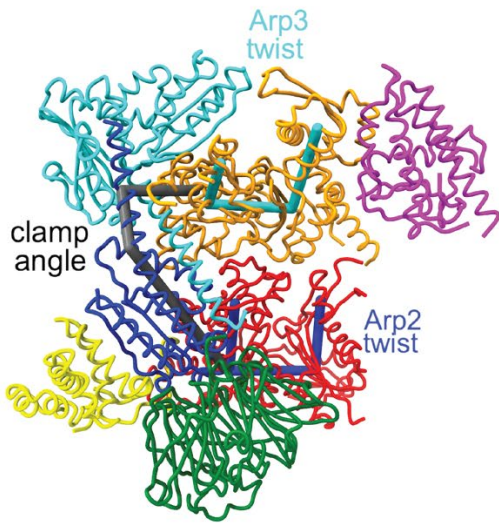
**Figure S7. Contacts between Arp2/3 complex and the nucleated actin filament are nearly identical in linear and branched actin structures. (A)** Comparison of the branch junction model (left) to the structure of Dip1-activated Arp2/3 complex bound to the pointed end of a linear actin filament (PDB ID code 6W17, right). Arrowheads mark the interface between Arp2/3 complex and the pointed end of the nucleated actin filament. **(B)** Two views of a structural overlay of the C $\alpha$  atoms from Arp2, Arp3, and the first two actin subunits in the nucleated actin filament in the branch junction model with the same subunits the Dip1-activated Arp2/3 complex structure. The Dip1-activated structure is shown in grey. Arrowheads mark the interface between Arp2/3 complex and the pointed end of the nucleated actin filament.










**Figure S8. The Arp3 C-terminus is released from the Arp3 barbed end groove in the branch junction structure.** Diagram shows the position of the Arp3 C-terminal tail in the branch junction model presented here (cyan) versus its position in the inactive Arp2/3 complex (blue). The inactive C-terminal tail was modeled by overlaying Arp3 in 4JD2 onto subdomains 1 and 2 of Arp3 in the branch junction structure.



INACTIVE



	ARPC2
	Arp3
	Arp2
	ARPC1
	ARPC3
	ARPC4
	ARPC5

ACTIVE

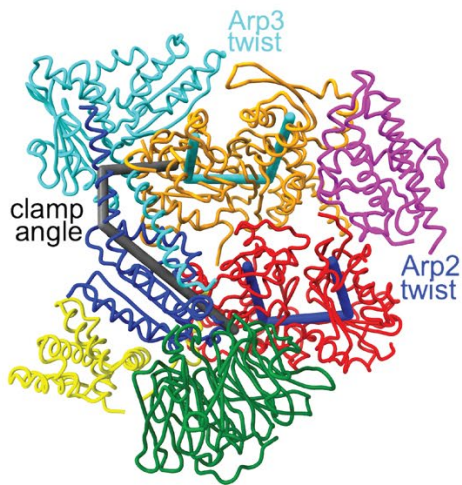
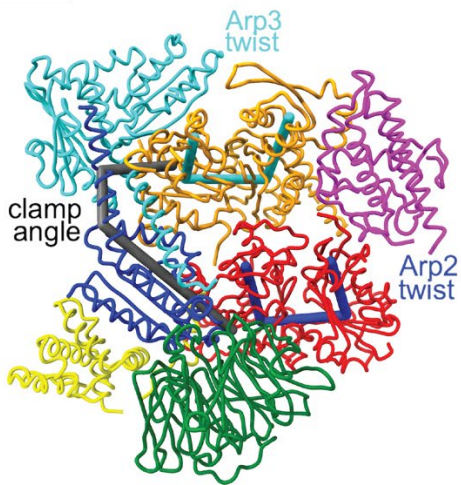


**Figure S9. Two major structural changes trigger branching nucleation.** Stereo view of comparison of inactive (PDB ID code 4JD2) Arp2/3 complex to activated Arp2/3 complex at the branch junction, as depicted in Figure 4B. The major conformational differences, clamp twisting and flattening of each Arp, can be measured via three different dihedral angles.

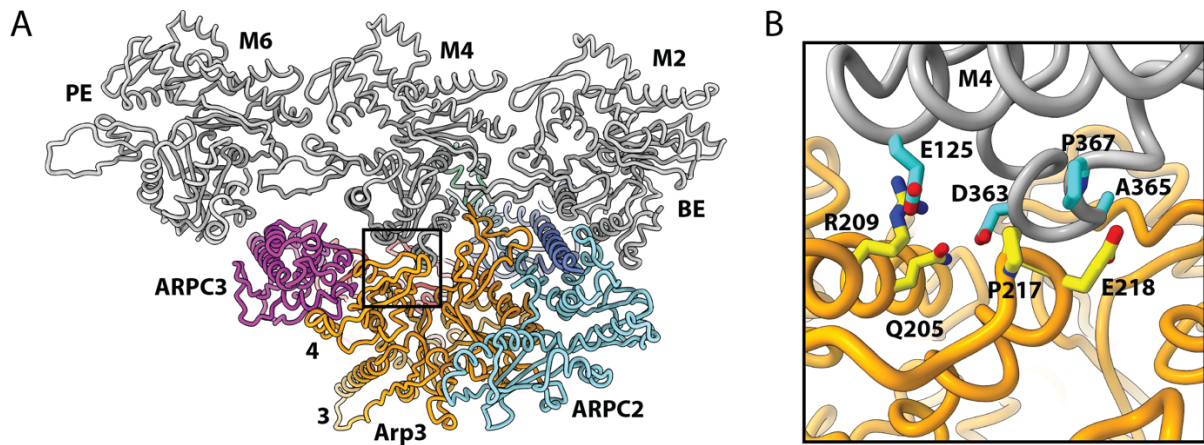


**Figure S10. Flattening of Arp3 increases contacts of Arp2/3 complex with the mother filament of actin. (A)** Overview of interactions of the top of the complex with one of the two protofilaments within the actin filament. Boxed region is shown in detail in panel B. **(B)** Close up of interactions between Arp3 and actin subunit M4 made possible by Arp3 flattening.

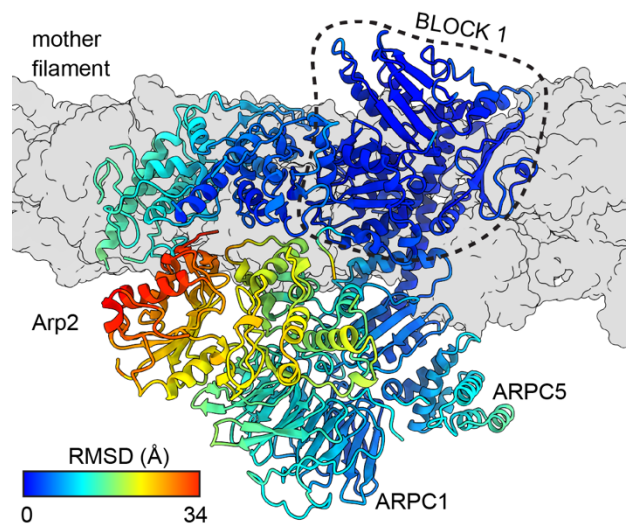


**Figure S11. The transition between splayed and short pitch conformations does not cause significant changes at the interface between Arp2/3 complex and the mother filament of actin.** Ribbon diagram of Arp2/3 complex at the branch junction colored by backbone RMSD to the inactive Arp2/3 complex (PDB ID code 4JD2). Active and inactive structures were superposed using C $\alpha$  atoms in block 1.

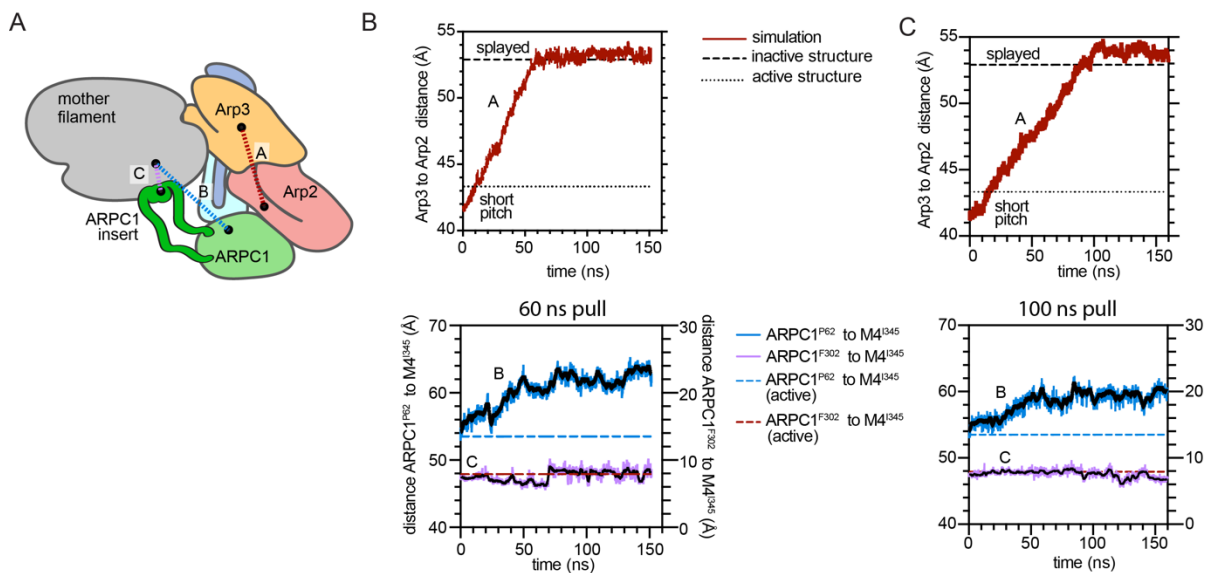


**Figure S12. The protrusion helix in the ARPC1 insert can engage the mother filament regardless of whether Arp2/3 complex is in the short pitch or the splayed conformation. (A)** Schematic showing key distances in molecular dynamics (MD) simulations plotted in panels B and C. **(B,C) Top -** Plot of distance A, which measures the distance between the centers of mass of Arp2 and Arp3 (inner subdomains, 3 and 4), versus simulation time. The centers of mass of Arp2 and Arp3 move apart as Arp2 transitions from the short pitch to splayed conformation. The equilibrated branch junction structure is pulled to the splayed conformation using an RMSD-based biasing force over 60 (panel B) or 100 (panel C) ns simulation time (see methods). The distance between Arp2 and Arp3 in the active (short pitch, flattened) conformation in the branch junction is shown with a dotted line, while the distance in the inactive (splayed, twisted) conformation is shown with a dashed line. **Bottom -** Plot of distances B and C, which measure the distance between the globular portion of ARPC1 or the protrusion helix and the mother filament versus simulation time. Dashed lines show the values of these distances in the branch junction structure presented here.

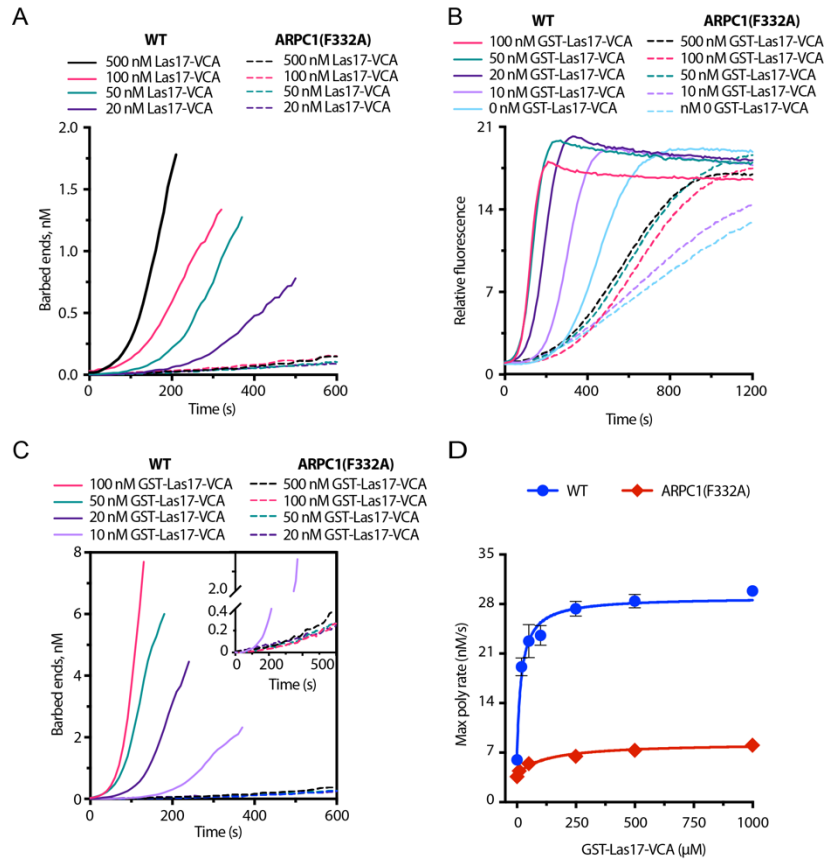


**Figure S13. The ARPC1 insert is important for activation of Arp2/3 complex by WASP proteins.** **(A)** Plot of concentration of barbed ends nucleated versus time for reactions containing wild-type or ARPC1(F332A) mutant and a range of concentrations of Las17-VCA. Time courses used to calculate the concentration of barbed ends are shown in Fig. 7B. **(B)** Time courses of pyrene actin polymerization for reactions containing 20 nM wild type or ARPC1(F332A) mutant Arp2/3 complex and the indicated concentration of the VCA segment of GST-tagged Las17 (GST-Las17-VCA). GST-tagged Las17-VCA was tested because some evidence suggests that WASP proteins oligomerize *in vivo* and biochemical data show differences in activation potency of monomeric versus dimeric WASP proteins (11, 12). **(C)** Plot of concentration of barbed ends nucleated versus time for reactions containing wild-type or ARPC1(F332A) mutant and a range of concentrations of GST-Las17-VCA. Time courses used to calculate the concentration of barbed ends are shown in panel B. **(D)** Quantification of the maximum polymerization rate from the data in panel B. Data points are averages of 3 replicates. Error bars show standard deviation, but are omitted if they are close to the size of the data point maker.

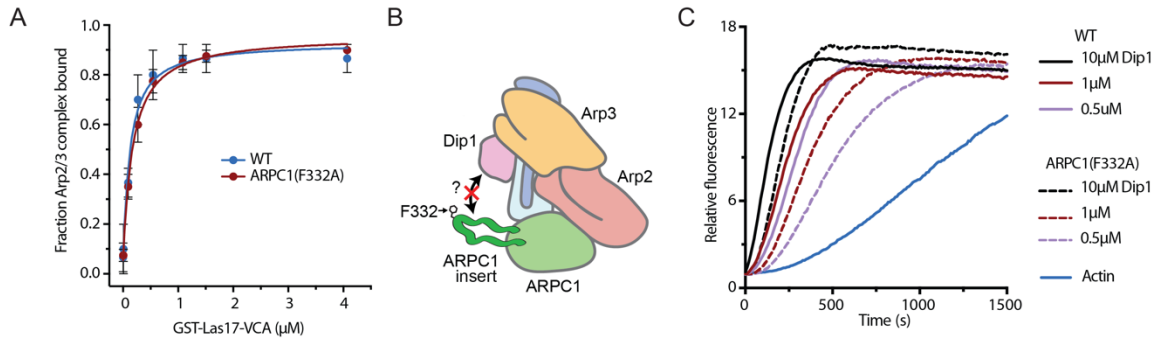


**Figure S14. Effects of mutation of F332 in the ARPC1 protrusion helix. (A)** Binding isotherm showing the fraction of 45 nM wild type or ARPC1(F332A) mutant bound to a range of concentrations of GST-Las17-VCA immobilized on glutathione agarose beads. **(B)** Schematic of Arp2/3 complex with bound Dip1 depicting a scenario in which the ARPC1 insert has no role in Dip1-mediated activation of the complex. **(C)** Time course of pyrene actin polymerization for reactions containing 20 nM wild type or ARPC1(F332A) mutant Arp2/3 complex and the indicated concentration of Dip1.



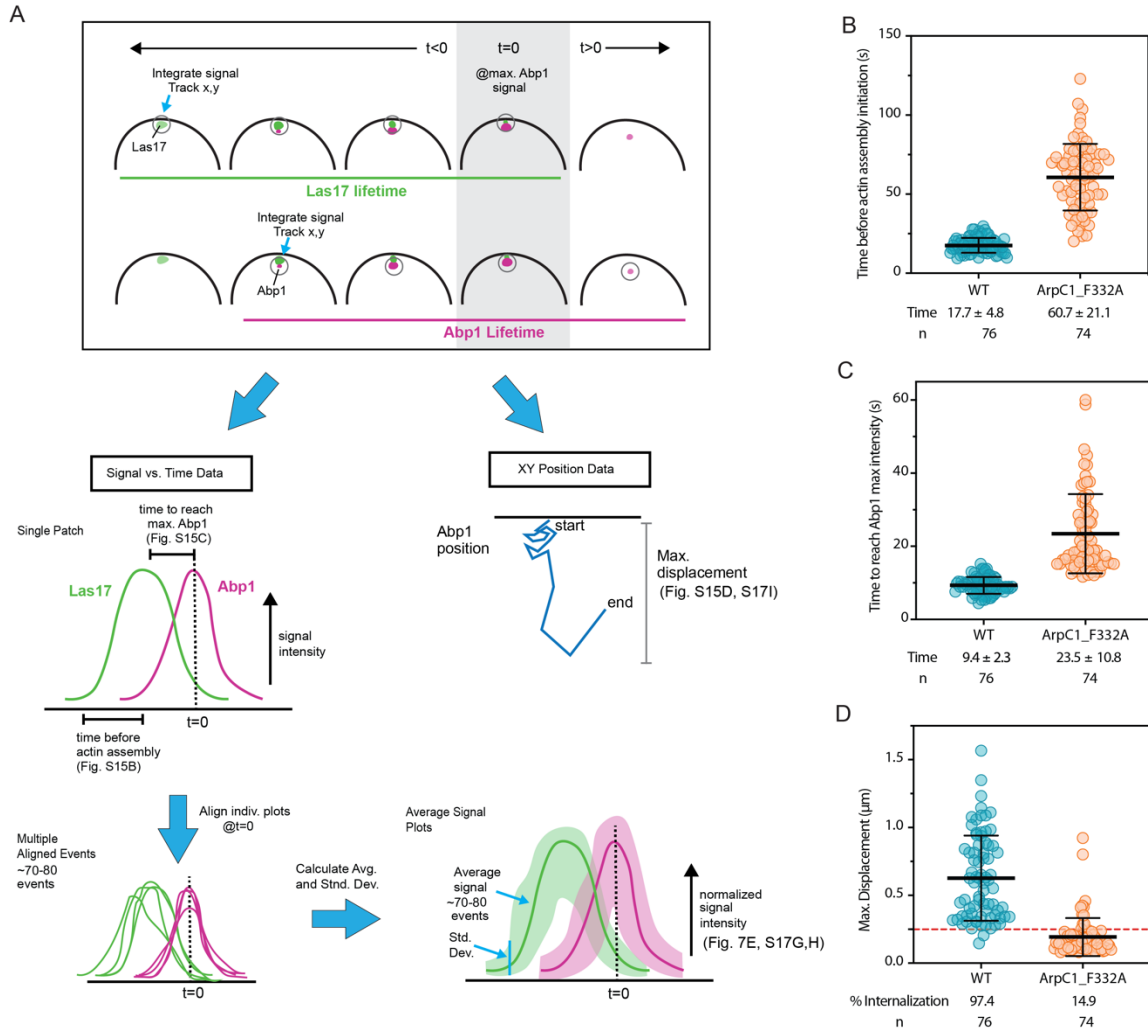


**Figure S15. Analysis of mNG-Las17 and Abp1-TagRFP-T dynamics in *S. cerevisiae*.**

(A) Schematic of data collection and analysis procedure. After background and photobleaching correction, we tracked the intensity and position of individual puncta of mNG-Las17 and Abp1-TagRFP-T. These data were used for all quantitative analysis of the WT, ARPC1(F332A) and Arp2(I38A, L39A, L51A) yeast strains. Please see methods for additional information. (C) Plot of the time between the first appearance of mNG-Las17 and Abp1-TagRFP-T in wild type and ARPC1(F332A) strain. Error bars show standard deviation. (D) Plot of the time to reach the maximum signal of Abp1-TagRFP-T in wild type and ARPC1(F332A) strain. Error bars show standard deviation. (E) Plot of the maximum distance from origin of Abp1-TagRFP-T in wild type and ARPC1(F332A) strain. Puncta that moved more than 0.25  $\mu\text{m}$  (red dashed line) were categorized as successful internalization events. Error bars show standard deviation.

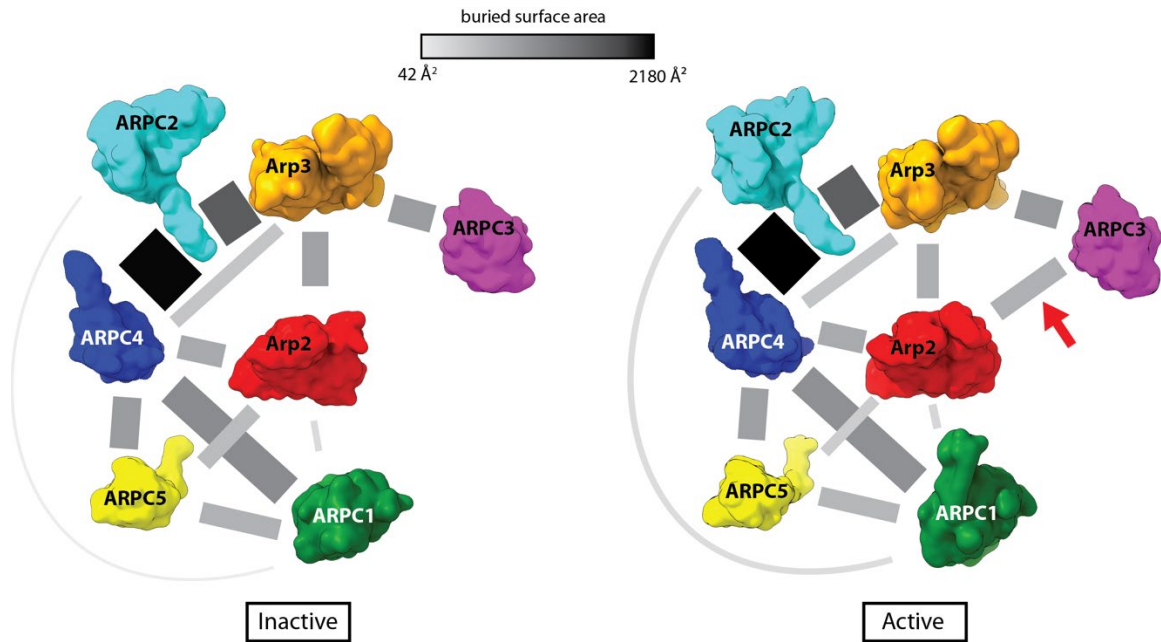


**Figure S16. Buried surface area between Arp2/3 complex subunits.** Left panel shows buried surface area between Arp2/3 complex subunits in the inactive conformation (PDB 4JD2). Both the thickness of the lines connecting the subunits and the grey value of the lines are proportional to the amount of buried surface area. Right panel shows the same representation for the active branch junction structure presented here. Red arrow shows the contact between Arp2 and ARPC3, which is not present in the inactive structure.



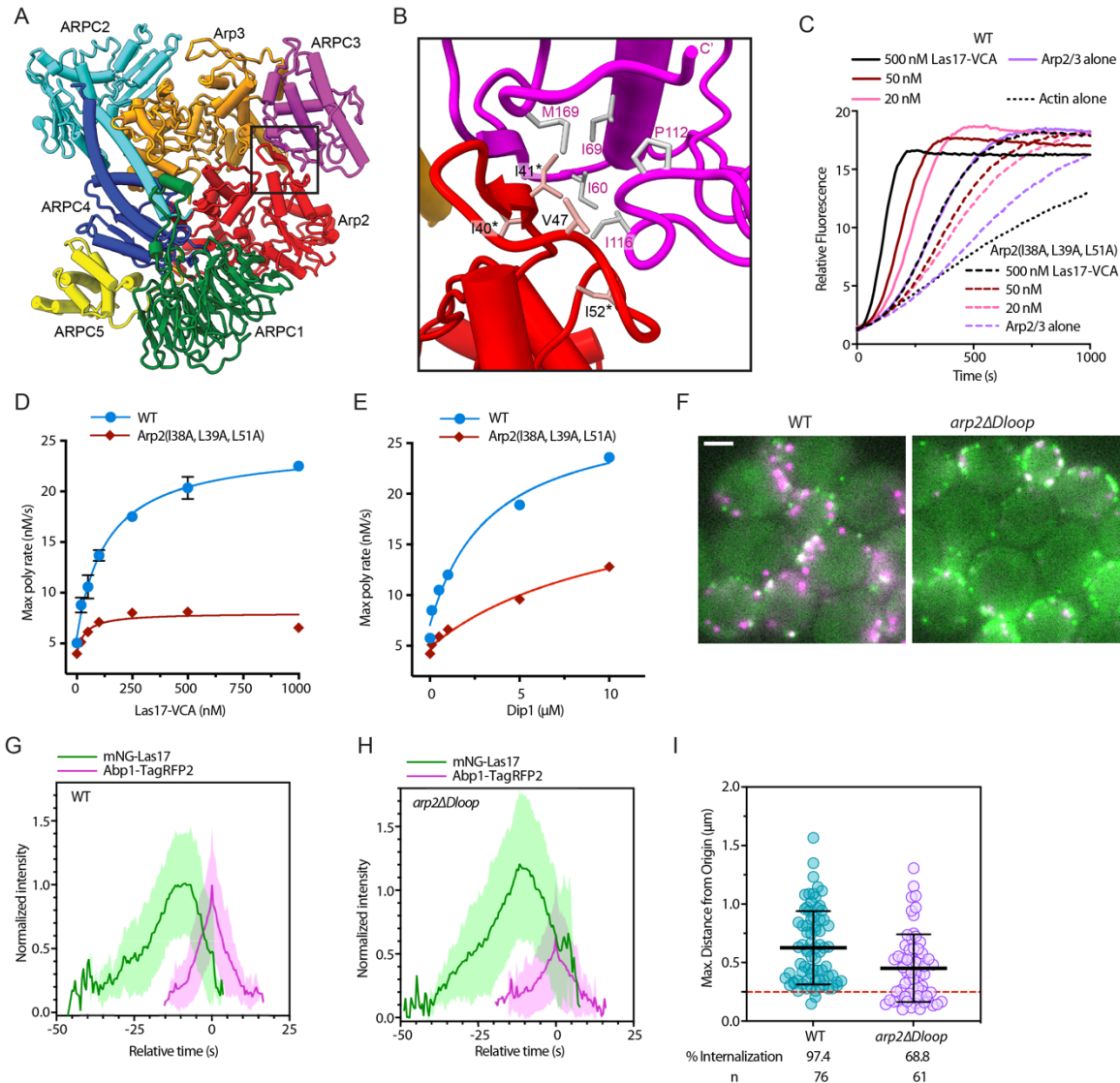


**Figure S17. The Arp2 D-loop makes contacts with ARPC3 that are important for branching nucleation and endocytic actin assembly.** (A) Structure of the branch junction with contact between Arp2 D-loop and ARPC3 boxed. (B) Close up of region boxed in panel A. Residues marked with asterisks were changed to alanine in the triple mutant. (C) Time courses of pyrene actin polymerization for reactions containing 20 nM wild type or Arp2(I38A, L39A, L51A) mutant Arp2/3 complex and the indicated concentration of the VCA segment of Las17 (Las17-VCA). (D) Quantification of the maximum polymerization rate from the data in panel C. Data points are averages of 3

replicates. Error bars show the standard deviation but are omitted if there are similar in size to the data point marker. **(E)** Plot of the maximum polymerization rate for reactions containing 20 nM wild type or Arp2(I38A, L39A, L51A) mutant Arp2/3 complex and the indicated concentration of *S. pombe* Dip1. Each data point is a single replicate. **(F)** Widefield fluorescence images of cells expressing either wild type or Arp2 $\Delta$ D-loop Arp2/3 complex. The two images use the same minimum and maximum brightness values. Scale bar: 2  $\mu$ m. **(G)** Plot of the average intensity versus time showing the dynamics of the accumulation of mNG-Las17 and Abp1-TagRFP-T at endocytic sites in the wild type strain. Pairs of Abp1 and Las17 trajectories for 76 distinct endocytic events were aligned to the maximum intensity of Abp1-TagRFP-T and normalized to set the maximum average intensities for both fluorescence signals to 1.0. Shaded region shows the standard deviation. **(H)** Plot of the average intensity versus time showing the dynamics of the accumulation of mNG-Las17 and Abp1-TagRFP-T at endocytic sites in the Arp2 $\Delta$ D-loop strain (n=61). The intensity values were normalized using the conversion factors for the wild type strain. **(I)** Plot of the maximum distance each endocytic patch moved from its initial site of site of assembly on the cortex in the wild type and mutant strains. Failure to move at least 0.25  $\mu$ m (red dashes) indicates failed internalization of the actin network. Error bars show standard deviation.

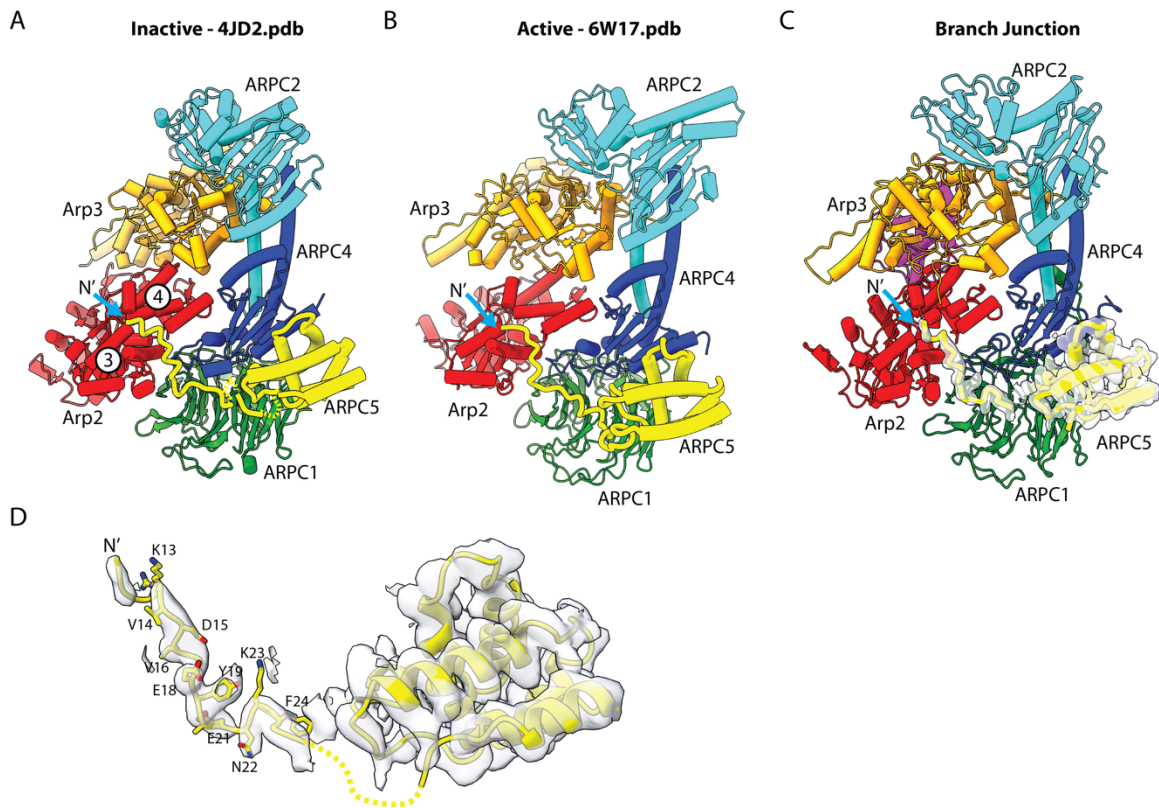


**Figure S18. The ARPC5 N-terminus makes identical contacts to Arp2/3 complex in the inactive versus the activated structure. (A)** Ribbon diagram of inactive Arp2/3 complex (PDB 4JD2) showing the position of the ARPC5 N-terminus. **(B)** Ribbon diagram of active Arp2/3 complex from the cryo-EM structure of Arp2/3 complex bound to the WDS-family activator Dip1 (PDB 6W17) showing the position of the ARPC5 N-terminus. **(C)** Ribbon diagram of active Arp2/3 complex from the cryo-EM structure of Arp2/3 complex at a branch junction presented here. The electron density for the ARPC5 subunit is shown in transparent grey. **(D)** Close up of the ARPC5 subunit from the branch junction structure presented here with electron density shown in transparent grey.

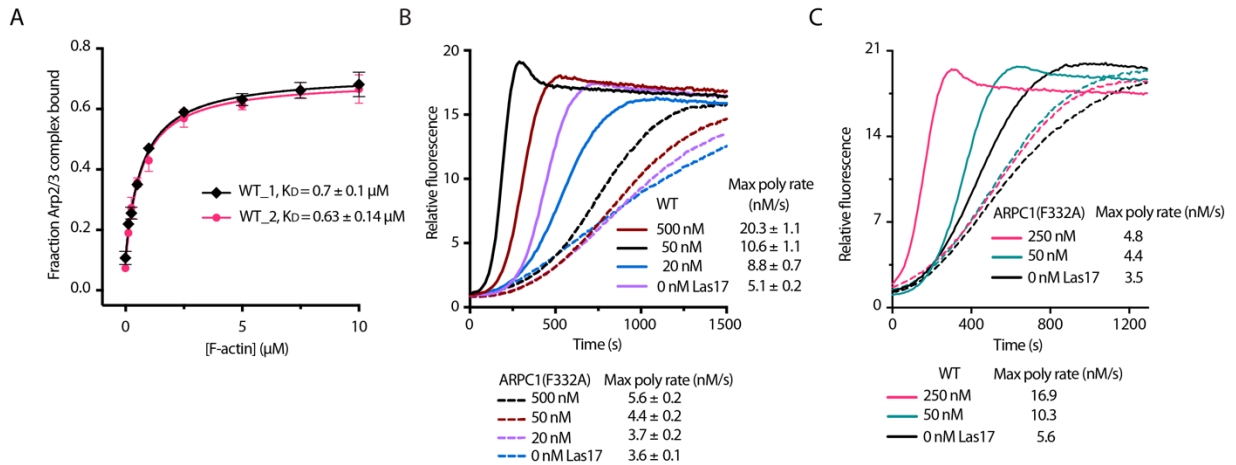


**Figure S19: Biochemical characterization of multiple preparations of wild type *S. cerevisiae* Arp2/3 complex.** (A) Actin filament copelleting assays using two different protein preparations of *S. cerevisiae* Arp2/3 complex. (B) Time courses of polymerization of pyrene-labeled actin shown in Fig7B, but with average maximum polymerization rates from each concentration of Arp2/3 complex indicated (n=3 individual assays with one preparation each of the WT and mutant complexes). (C) Time courses of polymerization of pyrene-labeled actin performed using the same preparation of Las17, but a different preparation of WT Arp2/3 complex than in panel B. The mutant complex used in this assay is the same preparation as in panel B.

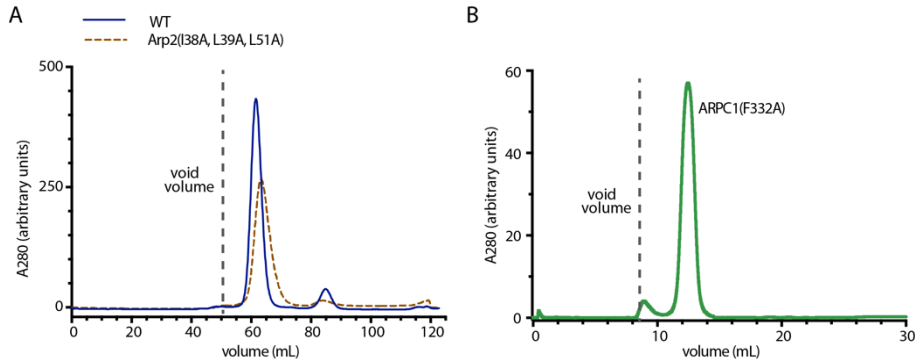


**Figure S20. Gel filtration elution profiles of *S. cerevisiae* Arp2/3 complex show no evidence of aggregation or subunit dissociation. (A)** Plot of the absorbance at 280 nm versus elution volume for WT and Arp2(138A, L39A, L51A) Arp2/3 complexes. **(B)** Plot of the absorbance at 280 nm versus elution volume for ARPC1(F332A) Arp2/3 complex.

**Supplementary Table 1. Cryo-EM data collection, refinement, and validation statistics.**

Sample name	<b>Branch junction</b>		
EMDB ID	EMD- 26063		
PDB ID	7TPT		
Microscope	Talos Arctica		
Detector (Mode)	Falcon 3EC counting mode		
Voltage (kV)	200		
Magnification (nominal)	92,000x		
Total electron fluence (e <sup>-</sup> /Å <sup>2</sup> )	41.87	42.36	41.68
Electron flux (e <sup>-</sup> /pixel/sec)	0.75	0.76	0.75
Defocus range (µm)	-0.8 to -1.2	-0.8 to -1.2	-0.8 to -1.2
Pixel size (Å)	1.12	1.12	1.12
Total exposure time (sec)	70	70	70
Total fractions/micrograph	82	82	82
Exposure per fraction (e <sup>-</sup> /Å <sup>2</sup> /frame)	0.51	0.52	0.51
Micrographs collected (no.)	1196	5073	1167
Total extracted particles (no.)	2,290,562		
Particles used for 3D analyses (no.)	758,265		
Final refined particles (no.)	127,093		
Symmetry imposed	C1		
FSC 0.5 (masked/unmasked)	4.7 / 8.8		
FSC 0.143 (masked/unmasked)	3.9 / 4.8		
FSC Sphericity	0.827		
Local resolution range (Å)	3.5 - 6		
Map Sharpening <i>B</i> factors (Å <sup>2</sup> )	-70		

<b>Model composition</b>	
Non-hydrogen atoms	50760
Protein residues	7202
Ligands	62
<b>Refinement</b>	
Refinement package (s)	Phenix
Map Correlation Coefficient	
Global	0.62
Local	0.61
<b>R.m.s. deviations</b>	
Bond lengths (Å)	0.010
Bond angles (°)	1.221
<b>Validation</b>	
EMRinger score	1.18
MolProbity score	1.78
Clashscore	9.70
Poor rotamers (%)	0.45
Cβ deviations (%)	0.30
<b>Ramachandran plot</b>	
Favored (%)	95.99
Allowed (%)	4.01
Disallowed (%)	0.00
CaBLAM outliers (%)	1.88

**Supplementary Table 2. *Saccharomyces cerevisiae* strains used in this study**

Strain	Source	Genotype
ScBN002-5	(13)	<i>MATa, ura3, his3, leu2, lys2, trp1, Δarp2::TRP1 pDW6(Arp2::URA3)</i>
ScBN020	(13)	<i>MAT?, ura3, his3, leu2, lys2, trp1 Δarp2::TRP1 Δarp3::HIS pBN002 (Arp3/pRS315) pBN001(Arp2/pRS117)</i>
ScBN156-6	(14)	<i>MATα, Darc40::TRP1, ARC40(F332A)::URA3, his3, trp1, lys2</i>
ScBN275/ DDY2918	<i>D. Drubin</i>	<i>MATα/α, ura3-52/ura3-52, his3Δ200/his3Δ200, leu2-3,112/leu2-3,112, lys2-801(oc)/+, ade2-1/+, Δarp2::HIS3/+</i>

ScBN344	<i>this study</i>	<i>MAT<math>\alpha</math>, Darc40::TRP1, ARC40(F332A)::URA3, his3, trp1, lys2, ABP1-TagRFP-T::kanMX6, natMX6::mNeonGreen-Las17</i>
ScBN434	<i>this study</i>	<i>MAT<math>\alpha</math>, ARP2::URA3, leu2, <math>\Delta</math>arp2::HIS3, Abp1-TagRFP-T::kanMX6, natMX6::mNG-Las17</i>
ScBN435	<i>this study</i>	<i>MAT<math>\alpha</math>, ARP2<math>\Delta</math>Dloop (<math>\Delta</math>39-55)::URA3, leu2, <math>\Delta</math>arp2::HIS3, Abp1-TagRFP-T::kanMX6, natMX6::mNG-Las17</i>
ScBN436	<i>this study</i>	<i>MAT<math>\alpha</math>, ARP2<math>\Delta</math>Dloop (<math>\Delta</math>39-55)::URA3, leu2, <math>\Delta</math>arp2::HIS3</i>
ScBN455	<i>this study</i>	<i>MAT<math>\alpha</math>, ura3, his3 leu2 lys2, trp1, ade? <math>\Delta</math>arp2:TRP1 pBN168 (Arp2 I38A, L39A, L51A::LYS2)</i>

## Supplementary movie legends

**Movie S1. Two major structural changes allow the Arp subunits to mimic a filamentous actin dimer during branching nucleation.** Morph between inactive Arp2/3 complex (PDB ID code 4JD2) and active Arp2/3 complex at the branch junction structure presented here. Structures were overlaid based on the backbone atoms of the globular portion of ARPC2 (blue ribbon representation) and subdomains 1 and 2 of Arp3 (orange ribbon representation, left half of molecule comprised subdomains 1 and 2). Residues that were not present in both structures were not included in the morph.

**Movie S2. Arp2 flattens during activation of branching nucleation.** Morph between inactive/twisted Arp2 (PDB ID code 4JD2) and active/flattened Arp2 from the branch junction structure presented here. Structures were overlaid based on subdomains 1 and 2 of Arp2 (subdomains are numbered 1-4). Residues that were not present in both structures were not included in the morph.

**Movie S3. Arp3 flattens during activation of branching nucleation.** Morph between inactive/twisted Arp3 (PDB ID code 4JD2) and active/flattened Arp3 from the branch junction structure presented here. Structures were overlaid based on subdomains 1 and 2 of Arp3 (subdomains are numbered 1-4). Residues that were not present in both structures were not included in the morph.

**Movie S4. The Arp2/3 complex can transform from splayed to short pitch conformations without major changes to interactions with mother filament of actin.** Video shows a morph between inactive Arp2/3 complex (PDB ID code 4JD2) and active Arp2/3 complex at the branch junction. Backbone atoms in block 1 of the inactive Arp2/3 complex were superposed onto the active complex before making the morph.



**Movie S5. Spinning disk confocal video of wild type *S. cerevisiae* cells expressing mNG-Las17 and Abp1-TagRFP-T.** Representative video showing endocytic events occurring in *S. cerevisiae* cells expressing wild type Arp2/3 complex. A time lapse of 80 seconds was collected at the medial plane of the cells. Images were acquired using 200 msec exposures for 488nm (mNG-Las17, right panel) and 561 (Abp1-TgRFP-T, center panel) channels, and deconvolved using NIS Elements. Scale bar: 3  $\mu$ m

**Movie S6. Spinning disk confocal video of ARPC1(F332A) *S. cerevisiae* cells expressing mNG-Las17 and Abp1-TagRFP-T.** Representative video showing endocytic events occurring in *S. cerevisiae* cells expressing ARPC1(F332A) complex. A time lapse of 80 seconds was collected at the medial plane of the cells. Images were acquired using 200 msec exposures for 488nm (mNG-Las17, right panel) and 561 (Abp1-TgRFP-T, center panel) channels, and deconvolved using NIS Elements. Scale bar: 3  $\mu$ m

## **Supplemental Methods:**

### **Protein purification**

*Bos taurus* Arp2/3 complex was purified from calf thymus as previously described (15). Dip1 was purified as described in Balzer, et al. (16). His-tagged mouse capping protein ( $\alpha$ -1,  $\beta$ -2) in a pRSF Duet vector (a gift from David Kovar) was purified as described in Shaaban, et al. (17). SPIN90(269-722) was purified as described in Luan, et al. (18). *Mus musculus* cortactin (1-336) was purified as described in Helgeson, et al. (19). Actin was purified from rabbit skeletal muscle acetone powder (Pel Freeze, #41995) and labeled with pyrene as described in Balzer, et al. (16). *Saccharomyces cerevisiae* Arp2/3 complexes (mutant and wild type) were purified using a protocol similar to that described by Narvaez-Ortiz, et al. (20). Briefly, strains ScBN020, ScBN156-3, ScBN436 or ScBN455 were inoculated from a plate into a 50 mL starter culture of minimal medium plus adenine lacking leucine, and lysine, and grown at 30 °C for approximately 6-8 hours. An appropriate volume of starter culture was diluted in YPAD to give an initial OD<sub>600</sub> of ~0.02 before growing for 19-21 additional hours. When the cultures reached OD<sub>600</sub> of 9-10, an

additional 25g/L of YPD powder was added and cells were grown for 2 more hours, then pelleted, washed in lysis buffer (20mM Tris pH 8.0, 100 mM NaCl, 1mM EDTA, 1mM DTT, plus protease inhibitor cocktail). Cells were lysed in a Microfluidics model 110EH at 25,000 psi using 5-7 passes through the chamber. PMSF was added to 1 mM immediately after lysis, and the lysate was clarified by spinning for 25 min at 9000 rpm in a JLA10.5 rotor and then for 1.25 hr at 40K RPM in a Ti45 rotor. After clarification, the supernatant was filtered through cheesecloth and protein precipitated with ammonium sulfate (313g/L) before spinning at 38K RPM in a Ti45 rotor. The sample was resuspended and then dialyzed overnight in PKME buffer (25mM Pipes, 50mM KCl, 1mM EGTA, 3mM MgCl<sub>2</sub>, 1mM DTT, 0.1mM ATP – pH adjusted to 7.0 with KOH). The sample was then loaded on a glutathione sepharose column charged with GST-N-WASP-WA, washed, and then eluted with a salt gradient (low salt: 200mM NaCl, 20mM Tris-HCl pH 8.0, 1 mM DTT; high salt: 1M NaCl, 20mM Tris-HCl pH 8.0, 1 mM DTT). Pooled fractions were concentrated in a Vivaspin turbo 15 unit (50 MWCO, Sartorius) and diluted in 20 mM Tris-HCl pH 8.0, 1 mM DTT to reduce the salt concentration to approximately 75 mM before loading onto a Resource Q column. The sample was washed on the column before eluting with a salt gradient of 100-500 mM NaCl. Pooled fractions were concentrated and run over a Superdex200 gel filtration column before repooling and concentrating. Protein concentration was measured using an E290 of 154,000 M<sup>-1</sup>cm<sup>-1</sup>. Purified *S. cerevisiae* Arp2/3 complex was flash frozen and stored at -80 °C. The biochemical data in Figure 7, S13, S14, and S17 were collected with a single preparation of each mutant *S. cerevisiae* Arp2/3 complex. No additional preparations of the mutants were tested. However, multiple preparations of the wild type Arp2/3 complex suggest there is little variation among preparations (Fig. S19).

The GST-N-WASP-VCA used for affinity purification was purified as described in Doolittle, et al. (21). GST-tagged Las17(529-633) (GST-Las17-VCA) was overexpressed in BL21(DE3) *E. coli*. Cells were lysed by sonication and clarified supernatant was run over a glutathione sepharose 4B column, washed and eluted with glutathione. Eluted protein was passed over a Resource Q ion exchange column and eluted over a gradient of 100-600 mM NaCl in a buffer containing 10 mM Tris-HCl pH 8.0 and 1 mM DTT. Pooled fractions were diluted in 20 mM Tris-HCl pH 8.0, 1 mM DTT to bring the NaCl concentration to 50 mM, concentrated and flash frozen. The concentration of GST-Las17-VCA was determined by absorbance and 280 nm using an extinction coefficient of 48610 M<sup>-1</sup>cm<sup>-1</sup>.

To produce Las17-VCA without a GST tag, the same protocol was followed, except that the eluted protein from the affinity step was cleaved with tobacco etch virus protease overnight before running the ion exchange step the next day. In addition, the cleaved Las17-VCA was run over a Superdex75 gel filtration column before concentrating and flash freezing. The concentration of Las17-VCA was determined by absorbance and 280 nm using an extinction coefficient of  $5500 \text{ M}^{-1}\text{cm}^{-1}$ . N-WASP-VCA without a GST tag was purified using the same protocol as cleaved Las17-VCA, except that the gradient in the Resource Q column was 140-800 mM NaCl. The purity of all proteins used in this study was verified by SDS-PAGE (Fig. S1A).

### **Sample preparation for electron microscopy**

To generate branched actin filaments for imaging,  $1.5 \mu\text{M}$  *Bos taurus* Arp2/3 complex,  $0.25 \mu\text{M}$  SPIN90,  $6 \mu\text{M}$  N-WASP-VCA,  $1.5 \mu\text{M}$  cortactin,  $9 \mu\text{M}$  *Oryctolagus cuniculus* skeletal muscle actin monomers and  $0.6 \mu\text{M}$  *Mus musculus* capping protein were mixed in an order described below, in buffer containing 20 mM HEPES pH 7.5, 50mM KCl, 1mM EGTA, 1mM  $\text{MgCl}_2$ , 0.2 mM ATP and 1 mM DTT. In order to image multiple branched actin junctions in vitrified cryo-EM samples, we ensured the formation of multiple short branched-actin filaments as described here. We initiated the reconstitution by first mixing Arp2/3 complex, SPIN90 and N-WASP-VCA together, followed by addition of one-tenth of the final concentration of actin monomers and one third capping protein. Subsequently, we added actin monomers in nine batches with incubation interval of 20 minutes at room temperature per batch. The remaining capping proteins were equally divided and added into the mixture during the third and seventh time of actin monomer addition. After the tenth incubation, we added cortactin, and allowed twenty minutes incubation before the addition of phalloidin to a final concentration of  $10 \mu\text{M}$ .

Grid vitrification for cryo-EM was performed in a  $4 \text{ }^\circ\text{C}$  cold room which maintained relative humidity between 90% and 95% to prevent sample dehydration.  $4 \mu\text{l}$  of the sample was added to a freshly plasma cleaned UltrAuFoil R1.2/1.3, 300-mesh gold grid (Quantifoil Micro Tools GmbH). Excess sample was removed by manually blotting each grid for 4 seconds from the rear side of the grid using a glass fiber filter (grade 691, VWR), and the grid was immediately flash-frozen in liquid ethane at  $-179 \text{ }^\circ\text{C}$ . The vitrification process was carried out using a custom-built manual plunge freezing device. Pipetting of the sample

during preparation and application on grids were performed using trimmed pipette tips to reduce the amount of shear force at the orifice to prevent complex disassembly.

### **Electron microscopy data acquisition**

Cryo-EM data were collected on a Thermo Fisher Scientific Talos Arctica transmission electron microscope operated at 200 kV. A Falcon 3EC direct electron detector (Thermo Fisher Scientific) was used to collect dose-fractionated movies in electron-counting mode. Three datasets were collected using EPU automated data acquisition software (Thermo Fisher Scientific) at a nominal magnification of 92,000x corresponding to a physical pixel size of 1.12 Å/pixel. In total 7,436 micrographs were collected from multiple data sets. Each micrograph comprised of 82 dose-fractionated frames collected over 70 seconds. Data were acquired at nominal defocus varying between -0.8 µm and -1.2 µm. To obtain multiple views of branched actin-junctions, data were collected by tilting grids (alpha-tilt) to 40 degree, 36 degree, 30 degree, 25 degree, 15 degree, -20 degree, -33 degree and also without tilting. The majority of the micrographs were collected at intermediate tilts as opposed to the untilted (0 degree) and the highest tilt (40 degree) angles. The three datasets comprised of 1,196 micrographs collected with an accumulated exposure dose of 41.87 e<sup>-</sup>/Å<sup>2</sup>; 5,073 micrographs with an accumulated exposure dose of 42.36 e<sup>-</sup>/Å<sup>2</sup>; and 1,167 micrographs with an accumulated exposure dose of 41.68 e<sup>-</sup>/Å<sup>2</sup>, respectively.

### **Image processing**

Cryo-EM data processing was carried out using the Cryosparc v2 processing suite (22). Movie frames for each micrograph were aligned using full-frame motion correction followed by patch motion correction. During this step beam-induced per-particle motion correction and dose-dependent radiation damage compensation over spatial frequencies were performed before averaging signals from all movie frames for each motion-corrected micrograph. Contrast Transfer Function (CTF) parameters were estimated using patch CTF estimation algorithm. 100 micrographs were then removed due to poor fit of CTF at high resolution and for those having severe astigmatism. Template-free blob picker was used for initial round of particle picking. These particles were subjected to 2D classifications, and class averages corresponding to different views of branched actin-junction and centered relative to the 2D box, were selected as templates for subsequent

template-based particle-picking. 2,290,562 particles corresponding to branched-actin junction that were picked using template-picking program were subsequently extracted from micrographs with box size of 368 pixels. 2D classification was performed on this set of particles. After removing particles belonging to classes that do not represent branched-actin junctions, a new stack of 758,265 particles were retained. Repeated iterations of *ab-initio* reconstructions with multiple classes were performed using this stack of particles. Subsequently 157,873 particles from *ab-initio* reconstructions, corresponding to branched-actin junctions were pooled for downstream data processing. These particles were then subjected to homogeneous 3D reconstruction using the best resolved *ab-initio* volume as the initial 3D reference. Particles were then subjected to local-motion correction to accurately correct for per-particle beam-induced motions. These local-motion-corrected particles were then classified by three rounds of heterogeneous reconstruction with 2, 3, and 4 classes respectively. 127,093 particles from the best resolved three 3D classes from the heterogeneous reconstruction rounds were pooled together to form a new particle stack. Global and local CTF refinements were performed on these particles for accurate, per-particle CTF correction during CTF refinement steps. Homogeneous reconstruction with local refinement resulted in a 3.9 Å resolution final 3D reconstruction of the branched-actin junction. The local resolution of the final map varied between 3.5 Å and 6 Å, and this was estimated using the local resolution estimation program in CryoSPARC. 3DFSC server (23)(<https://3dfsc.salk.edu>) was used for estimation of directional Fourier Shell Correlation (FSC). The 3D FSC curve indicates that the final reconstruction has moderate anisotropic resolution (Fig S1F) due to some of the Euler angles having limited projections. This did not result in any obvious distortions or artefacts in the map (Fig. 1A,1C,S1E,S3) that limited our ability to resolve individual subunits or hampered our interpretation of map for atomic model building. We do not observe any obvious trend of particles being eliminated significantly from higher alpha-tilt angles to the final reconstructed map. However, the contribution from the highest alpha-tilt angle (40 degrees) was the lowest in the final reconstructed map compared to the other alpha-tilts (Fig S2B). The final reconstructed map was sharpened with a B-factor of 70 Å<sup>2</sup>. Local sharpening of the map along with denoising was performed using DeepEMhancer program (24). These maps were used for final atomic-model building (Table 1).

## Model Building

Structures of *Bos taurus* Arp2/3 complex bound with *Mus musculus* GMF (PDB 4JD2) and *Oryctolagus cuniculus* ADP-actin filament (PDB 3J8I) were used as initial models for the Arp2/3 complex and actin. Individual subunits were extracted from these models and were rigid body fitted into the map using UCSF Chimera (25) to generate an initial composite model. This model was then flexibly fitted into the map using Namdinator web server (<https://namdinator.au.dk>) (26). Due to the relatively poor map densities for the regions corresponding to the actin subunits M-1 (chain U), M0 (chain T), M7 (chain M), M8 (chain L), D3 (chain J), and D4 (chain K), the side chain models of these subunits were truncated to C $\beta$  to reflect structural flexibility. Ligands, including ADP, magnesium, and phalloidin, were manually added into the model using COOT (27). The generated model for the complex was subjected to multiple rounds of real space refinement in Phenix (28). Geometry and rotameric outliers were manually fixed in COOT and then iteratively refined in Phenix to generate the final model. Model validation was performed using the Molprobrity server (<http://molprobrity.biochem.duke.edu/>) (29) and the PDB validation server (<https://validate-rcsb-1.wwpdb.org/>) (30) (Supplementary Table 1).

### Biochemical Assays

Actin filament copelleting assays were carried out as described in Luan, et al. (18). Briefly, actin filaments assembled from rabbit skeletal muscle actin were incubated with 60 nM wild type or ARPC1(F332A) *S. cerevisiae* Arp2/3 complex for 15 min at room temperature before centrifuging at 85 K in a TLA100 rotor at 22 °C for 20 min. The supernatant was removed and analyzed by an enzyme-linked immunosorbent assay as follows. Samples (10  $\mu$ L of each supernatant plus 40  $\mu$ L of 50 mM carbonate buffer pH 9.4) were incubated in a 96-well plate for 1 hr at room temperature. The plate was blocked with 5% milk for 1.5 hrs, incubated with  $\alpha$ -Arp3 in goat antibody (sc-11973, 1:1500) for 15 min, followed by incubation with  $\alpha$ -goat HRP (ab97110, 1:10,000) for 15 min. The plate was then washed 4x with TBST before adding 100  $\mu$ L TMB substrate (Thermo Scientific). The reaction was quenched after 15 – 30 min with 100  $\mu$ L 0.18 M H<sub>2</sub>SO<sub>4</sub>. The absorbance at 450 nm was used to determine the concentration of unbound Arp2/3 complex. The binding isotherm was fit using the following equation:

$$\frac{[RL]}{[R]_{total}} = \frac{[L]_{total} + [R]_{total} + K_D - \sqrt{(-[L]_{total} - [R]_{total} - K_D)^2 - 4[L]_{total}[R]_{total}}}{2[R]_{total}}$$

Where [R] is the concentration of Arp2/3 complex, [L] is the concentration of actin filaments, and [RL] is the concentration of Arp2/3 complex bound to actin filaments. We note that the fraction of Arp2/3 complex bound to actin filaments does not reach 100% in either binding reactions containing the wild type or the mutant complex. This is unlikely to be due to aggregation or misfolding of the complex during purification, because (a) gel filtration of the complexes showed no indication of aggregation or dissociation of the complex (Fig. S20), and (b) incomplete binding at saturation has been observed in actin filament copelleting assays in many different studies using Arp2/3 complex purified from different species with different protocols (7, 13, 31, 32).

Pyrene actin polymerization assays were carried out using rabbit skeletal muscle actin as described in Balzer et al. (16). The change in relative fluorescence over time was converted to a rate of actin polymerization assuming a critical concentration of actin of 0.1  $\mu\text{M}$ . Plots of average maximum polymerization rate versus concentration were fit to the following equation:

$$rate = rate_0 + \frac{[Las17 - VCA](rate_{max})}{[Las17 - VCA] + K_{1/2}}$$

Where  $rate_0$  is the maximum polymerization rate in the absence of Las17-VCA,  $rate_{max}$  is the maximum polymerization rate at saturating concentrations of Las17-VCA, and  $K_{1/2}$  is the concentration of Las17-VCA required to reach a maximum polymerization rate that is half the saturating value.

The instantaneous concentration of barbed ends in the reaction was calculated using an equation derived with the assumption that pointed end elongation was negligible:

$$[barbed\ ends] = \frac{elongation\ rate}{11.6\mu\text{M}^{-1}\text{s}^{-1}[monomer]}$$

To measure the binding affinity of Arp2/3 complex for Las17, Glutathione agarose beads (GoldBio) were incubated with a range of concentrations (20 nM-5  $\mu\text{M}$ ) of GST-Las17-VCA or GST alone for 1 hr at 4 °C in a nutator. Beads were washed 4 times with 140 mM NaCl, 20 mM Tris pH 8.0, 2 mM EDTA, and 1 mM DTT, and then equilibrated in 1 x KMEI/ATP (50 mM KCl, 10 mM Imidazole pH 7.0, 1 mM  $\text{MgCl}_2$ , 1 mM EGTA, 0.2 mM ATP, and 1mM DTT). Charged beads were incubated with 45 nM wild type or mutant Arp2/3 complex in 1xKMEI/ATP for 30 min at 22 °C. Samples were centrifuged in tabletop

centrifuge to pellet beads, and supernatant was removed and analyzed by SDS-PAGE followed by western blotting using an  $\alpha$ -Arp3 antibody (1:1000 dilution of Santa Cruz sc-11973). Binding isotherms were fit using the equation described for the actin filament copelleting assay, except [L] was the GST-Las17-VCA concentration.

### **Yeast strain construction**

Budding yeast strains used in this study are listed in Supplementary Table 2. To generate strain ScBN344, previously described strain ScBN156-3 was transformed with a cassette to tag the N-terminus of Las17 with mNeonGreen and mark it with NatMX6, and a second cassette to tag the C-terminus of Abp1 with TagRFP-T and mark it with KanMX6 (14, 33, 34).

To construct strain ScBN434, a diploid strain with one copy of Arp2 knocked out (ScBN275/DDY2918, a gift from David Drubin) was transformed with cassettes to tag Las17 and Abp1 with mNeonGreen and TagRFP-T, as described above. The resulting strain, once selected for its ability to grow on minimal media lacking uracil, histidine, G418, and nourseothricin was sporulated and selected against all four markers. Strains ScBN435 and ScBN436 were constructed using a similar strategy except that PCR was used to delete nucleotides encoding for residues 39-55 in the *ARP2* sequence in pBN51 before cleaving and transforming the plasmid into the diploid strain. The diploid was sporulated and selected against the appropriate selection markers to generate ScBN435 and ScBN436. Strains ScBN344, ScBN434, ScBN435, and ScBN436 were each verified by sequencing.

To construct strain ScBN455, which was used to purify the Arp2(I38A, L39A, L51A) Arp2/3 complex mutant, a previously described pRS317-based plasmid containing ARP2 plus 204 upstream and 168 downstream nucleotides was mutagenized to change three amino acids in the D-loop to alanine (I38, L39, and L51) (35). The resulting plasmid was transformed in ScBN002-5 and the strain was selected against minimal medium lacking lysine before plating on 5-FOA. Loss of the pDW6 plasmid from the transformed strain was verified by demonstrating no growth in minimal media lacking uracil and by isolating plasmids from the strain and attempting to amplify sequence specific to the pDW6 plasmid.

### **Live cell imaging and image analysis**



*Saccharomyces cerevisiae* cells were grown in YAPD for approximately 2 days while maintaining the optical density at 600 nm (OD) between 0.1-1.0 by dilution in fresh sterilized YAPD. Cultures were then diluted to OD 0.1 and grown for approximately 2.5 hrs before centrifuging, washing with minimal media and repelleting. Cells were resuspended in 50-200  $\mu$ L CMS media and then 3-4  $\mu$ L was added to a gelatin pad, covered with a coverslip, and sealed with a 1:1:1 mixture of petroleum jelly, lanolin and paraffin.

Images in Figure 7 along with the images used for measuring the number of mNeonGreen-Las17 patches in the cell were collected on a Nikon Ti2-E equipped with a Yokogawa CSU-W1 spinning disk and a Photometrics Prime BSI sCMOS camera. Images were collected using a 60x 1.49 NA objective using either a 50  $\mu$ m standard spinning disk (for Las17 puncta quantification) or a 50  $\mu$ m SoRa disk, which provided an additional 4x magnification (for Fig. 7D). Time course data were collected using 200 ms exposures for each channel (488nm and 561 nm) and the two channels were acquired every second. Data collected using the SoRa disk were deconvoluted using NIS Elements software. Data for Las17 puncta quantification were collected in 7-9  $\mu$ m Z-stacks with 0.2  $\mu$ m steps.

Images for tracking Las17 and Abp1 over time were collected on a GE DeltaVision Ultra widefield microscope equipped with a pco.edge 4.2 sCMOS camera and a 100x 1.4 NA objective lens. Images were collected using 100 ms exposure times for each channel (mNeonGreen and TagRFP-T). Data were collected continuously, with 0.45 s required to collect both channels. To process the images for tracking, the background was first subtracted in FIJI using a rolling ball radius of 70 pixels (36). The images were then corrected for photobleaching using the corr\_bleach macro (EMBL Heidelberg). The local background was subtracted using a median filter with a radius 1.5x the typical actin patch size (~12 pixels). Once the images were prepared, puncta of mNeonGreen-Las17 and Abp1-TagRFP-T were tracked with the TrackMate plugin in Fiji. Tracks output by TrackMate were manually inspected to ensure the puncta appear and disappear during the length of the video and that they are singular. The fluorescence signal of Abp1 and Las17 traces were normalized to set the average maximum signal to 1.0. Individual traces were overlaid and aligned based on the maximum intensity of Abp1-TagRFP-T. The percent internalization was calculated by counting the number of Abp1-TagRFP-T puncta that move 0.25 microns or more from their initial site of assembly at the cell cortex.

Images shown in Figure 7D,7F, and S17F are representative of (at least) 5 videos taken from 5 different cultures of 2 different isolates of WT or mutant strains. The analyses in Figure 7E, S15B, S15C, S15D, S17G, S17H, and S17I include data from (at least) 5 videos taken from 5 different cultures of 2 different isolates of WT or mutant strains.

### **Molecular dynamics simulation methods**

System construction for molecular dynamics simulations generally proceeded as described in Hocky, et al. (37). To study the activation transition of the Arp2/3 complex, we used VMD (38) to construct a simulation system which is a subset of the full junction model solved here, containing only the Arp2/3 complex and the mother filament of actin. ADP in Arp2 and Arp3 were replaced by ATP to represent a pre-activation state of the complex. Coordinating water was added within the nucleic acid binding pocket by aligning the nucleic acid in the junction model with one in an equilibrated system containing only one actin in the filamentous state (39). The system was placed in a box of water such that a minimum of 1.5 nm of water extended from each side of the protein. A small fraction of water molecules were removed and replaced with ions such that the system was neutralized and the resulting solution contained 50 mM KCl. Simulations were run using the CHARMM22+CMAP forcefield with TIP3P water. Energy minimization and equilibration steps were carried out in NAMD (40) in several stages following the procedure described in Hocky, et al. (37). The equilibrated system topology was then converted to run in GROMACS (41) for production MD simulations. runs. Before initiating the production runs, the system was run for an additional relaxation run of 10 ns, at which point—to prevent rotation in the simulation box and to prevent any changes at the filament ends from propagating through the mother filament—restraints of 1000 kJ/nm<sup>2</sup> were applied to backbone atoms in mother actin subunits corresponding to chains L, M, T and U. This restraint was used throughout the production simulations. Unbiased simulations of up to 400 ns of this system showed no significant rearrangements of Arp2/3 complex.

Transitions from a short pitch to splayed configuration of the complex were generated using the MOVINGRESTRAINT function of the PLUMED plugin library (42). We tried several approaches to move Arp2/3 complex toward its inactive configuration; the one which proved successful was to bias all pairwise distances between the centers of the Arp2/3 complex subunits (with the center being defined using the C $\alpha$  atoms in each subunit). Because there are 7 domains in the Arp2/3 complex, this results in (7 choose

2)=21 'collective variables' to bias in the simulation. A harmonic bias  $V$  was then added to the energy of the system of the form  $V = \sum_{i=1}^{21} \frac{1}{2} \kappa (d_i(X(t)) - d_i^{target}(t))^2$ , where  $d_i(X(t))$  is the distance between two domains measured from the position of the system at time  $t$  ( $X(t)$ ), and  $d_i^{target}(t)$  is a function that changes from an initial value to a final value linearly over time  $\tau$ , i.e.  $d_i^{target}(t) = d_i^{initial} \left(1 - \frac{t}{\tau}\right) + d_i^{final} \left(\frac{t}{\tau}\right)$ . The initial values for the restraints  $d_i^{initial}$  were taken from the equilibrated and relaxed simulation just described. The final target values  $d_i^{final}$  were measured from the PDB ID code 4JD2. After time  $\tau$ ,  $d_i^{target} = d_i^{final}$ . Successful transitions from this starting structure to an approximate inactive Arp2/3 complex structure could be generated using  $\kappa = 10000 \text{ kJ mol}^{-1} \text{ nm}^{-2}$ . Pulling simulations were performed over different durations  $\tau$ , with the slowest (150 ns) shown in Figure 6. We note that the dashed line in Figure 6 for the Arp2-Arp3 distance in the active model is taken directly from the branch junction model, before equilibration and relaxation. Additional simulations with 60 and 100 ns of pulling are shown in Figure S12.

### Structural Analysis

All structural analysis was carried out with PyMOL, Chimera, or ChimeraX (25, 43). Structure figures were made with ChimeraX (43). Buried surface area calculations were carried out with PISA protein interaction server (44). The blocks that describe the major rigid body motions that occur during activation are defined as follows:

Block 1: ARPC2 (chain D); 1-262, Arp3; 1-153, 375-418, ARPC4; 151-172

Block 2: ARPC2; 263-283, ARPC4; 1-150, ARPC5, ARPC1, Arp2; 151-351

Block 3: Arp3; 154-374, ARPC3

Block 4: Arp2; 1-150, 352-394

Blocks were defined based on the approximate boundaries of the rigid bodies that define the motion from the inactive to active conformations as determined by visual inspection of a structural morph. In the case of Arp3 and Arp2, block boundaries corresponded with the boundary between the inner (subdomains 3 and 4) and outer (subdomains 1 and 2) domains of the actin-related proteins. The block definitions are nearly identical to the rigid bodies identified by Dynom (85), except that (a) small flexible segments inserted within a domain are frequently not considered part of Dyndom-defined domain, as small rearrangement of these regions may prevent them from being well-superposed in the two

conformations being compared and (b) Dyndom did not detect flattening of Arp2 as a rigid body motion, so subdomains 1 and 2 of Arp2 were counted as part of subdomain 2 in the Dyndom analysis.

In addition to the structure presented here, the plot of Arp subunit twist angle versus distance  $x_2$  (Fig. 5B) includes the structures with the following PDB ID codes: 6W17, 4JD2, 1K8K, 2P9K, 1TYQ, 3DWL, 2P9I, 4XEI, 2P9I, 4XEI, 1U2V, 2P9N, 2P9P, 2P9S, 3DXK, 3DXM, 3UKU, 2P9I, 2P9U, 3RSE, 3UKR, 1J6Z, 1NWK, 6DJN, 6DJM, and 6DJO. Distance  $x_2$  is measured between V143 CA and T184 CA in *Bos taurus* Arp3, between I140 CA and F173 CA in *Bos taurus* Arp2, and between I136 CA and Y169 CA in rabbit skeletal muscle actin. The plot of the distance between Arp2 and Arp3 centers of mass versus the clamp dihedral (Fig. 4D) includes the branch structure plus PDB ID codes 6W17, 4JD2, 1K8K, 2P9K, 1TYQ, 3ULE, 6DEC, 3DWL, 6W18, 2P9I, 4XEI, 1U2V, 2P9N, 2P9P, 2P9S, 3DXK, 3DXM, 3UKU, 3RSE, and 3UKR. The clamp dihedral is defined by the following atoms: *Bos taurus* Arp2/3 complex; ARPC4 R32 CA, ARPC4 S147 CA, ARPC4 A157 CA, and Arp3 M93 CA, *S. pombe* Arp2/3 complex: ARPC4 R32 CA, ARPC4 S147 CA, ARPC4 A157 CA, and Arp3 W109 CA. To calculate distance between Arp3 and Arp2 for the plot in Figure 4D we used the centers of mass of the large (inner) domains of Arp2 and Arp3 (subdomain 3 and 4). This eliminated potential changes in the distance between the two subunits that could be caused by intra-subunit movement of the inner versus outer domains and removed potential inconsistencies in the calculation due to disordered/missing residues in the outer domain (subdomains 1 and 2) in most structures.

Structural morphs were made using the morph feature of ChimeraX. For the morph showing clamp twisting and subunit flattening (Movie S1-3), backbone atoms of block 1 of the inactive structure PDB ID code 4JD2 (ARPC2: 1-253; Arp3: 1-36, 60-153, 375-409) were superposed with the same atoms in the branch junction structure before making the morph. For the morphs showing subunit flattening in Arp3 and Arp2, backbone atoms of subdomains 1 and 2 of each Arp subunit were superposed with the corresponding atoms from the inactive structure of that subunit in PDB ID 4JD2.

To calculate the rise and twist angles presented in Figure S6D, we used the rotation\_axes.py script (<https://pymolwiki.org/index.php/RotationAxis>). Specifically we used the draw\_axis command to superimpose adjacent actin or actin-related proteins and recorded the output rotation and translation values for the superimposition. To calculate the branch-angle, the helical axis of the daughter and mother filament were generated

using the draw\_rotation\_axis python script in PyMOL. For the mother filament, the helical axis was defined by the rotation of chains L, N, P, R and T onto M, O, Q, S, and U. For the daughter filament, the helical axis was defined by the rotation of chains I and K onto chains J and H. The resulting vectors (MF: mother filament, DF: daughter filament) were used in the following equation to calculate the branch angle,  $\Theta$ .

$$\Theta = \arccos \frac{\text{vectorMF} \cdot \text{vectorDF}}{|\text{vectorMF}| |\text{vectorDF}|}$$

### Supplemental References Cited

1. R. E. Mahaffy, T. D. Pollard, Influence of phalloidin on the formation of actin filament branches by Arp2/3 complex. *Biochemistry* **47**, 6460–6467 (2008).
2. F. Merino, *et al.*, Structural transitions of F-actin upon ATP hydrolysis at near-atomic resolution revealed by cryo-EM. *Nat. Struct. Mol. Biol.* **25**, 528–537 (2018).
3. R. Dominguez, Nucleotide-dependent conformational changes in the actin filament: Subtler than expected. *Proceedings of the National Academy of Sciences* **116**, 3959–3961 (2019).
4. S. Z. Chou, T. D. Pollard, Mechanism of actin polymerization revealed by cryo-EM structures of actin filaments with three different bound nucleotides. *Proc. Natl. Acad. Sci. U.S.A.* **116**, 4265–4274 (2019).
5. Z. A. O. Durer, *et al.*, Structural States and Dynamics of the D-Loop in Actin. *Biophysical Journal* **103**, 930–939 (2012).
6. S. Pospich, F. Merino, S. Raunser, Structural Effects and Functional Implications of Phalloidin and Jasplakinolide Binding to Actin Filaments. *Structure* **28**, 437-449.e5 (2020).
7. S.-L. Liu, J. R. May, L. A. Helgeson, B. J. Nolen, Insertions within the actin core of actin-related protein 3 (Arp3) modulate branching nucleation by Arp2/3 complex. *J. Biol. Chem.* **288**, 487–497 (2013).
8. J. L. Morrell, M. Morphew, K. L. Gould, A mutant of Arp2p causes partial disassembly of the Arp2/3 complex and loss of cortical actin function in fission yeast. *Mol Biol Cell* **10**, 4201–4215 (1999).
9. F. Fäßler, G. Dimchev, V.-V. Hodirnau, W. Wan, F. K. M. Schur, Cryo-electron tomography structure of Arp2/3 complex in cells reveals new insights into the branch junction. *Nat Commun* **11**, 6437 (2020).

10. I. Rouiller, *et al.*, The structural basis of actin filament branching by the Arp2/3 complex. *J. Cell Biol.* **180**, 887–895 (2008).
11. S. B. Padrick, L. K. Doolittle, C. A. Brautigam, D. S. King, M. K. Rosen, Arp2/3 complex is bound and activated by two WASP proteins. *Proc. Natl. Acad. Sci. U.S.A.* **108**, E472-479 (2011).
12. S. B. Padrick, *et al.*, Hierarchical regulation of WASP/WAVE proteins. *Mol. Cell* **32**, 426–438 (2008).
13. B. Hetrick, M. S. Han, L. A. Helgeson, B. J. Nolen, Small molecules CK-666 and CK-869 inhibit actin-related protein 2/3 complex by blocking an activating conformational change. *Chem. Biol.* **20**, 701–712 (2013).
14. Q. Luan, A. Zelter, M. J. MacCoss, T. N. Davis, B. J. Nolen, Identification of Wiskott-Aldrich syndrome protein (WASP) binding sites on the branched actin filament nucleator Arp2/3 complex. *Proc. Natl. Acad. Sci. U.S.A.* **115**, E1409–E1418 (2018).
15. L. K. Doolittle, M. K. Rosen, S. B. Padrick, Purification of Native Arp2/3 Complex from Bovine Thymus. *Methods Mol Biol* **1046**, 231–250 (2013).
16. C. J. Balzer, *et al.*, Synergy between Wsp1 and Dip1 may initiate assembly of endocytic actin networks. *Elife* **9**, e60419 (2020).
17. M. Shaaban, S. Chowdhury, B. J. Nolen, Cryo-EM reveals the transition of Arp2/3 complex from inactive to nucleation-competent state. *Nat. Struct. Mol. Biol.* (2020) <https://doi.org/10.1038/s41594-020-0481-x>.
18. Q. Luan, S.-L. Liu, L. A. Helgeson, B. J. Nolen, Structure of the nucleation-promoting factor SPIN90 bound to the actin filament nucleator Arp2/3 complex. *EMBO J.* **37** (2018).
19. L. A. Helgeson, B. J. Nolen, Mechanism of synergistic activation of Arp2/3 complex by cortactin and N-WASP. *Elife* **2**, e00884 (2013).
20. H. Y. Narvaez-Ortiz, B. J. Nolen, Unconcerted conformational changes in Arp2/3 complex integrate multiple activating signals to assemble functional actin networks. *Curr Biol*, S0960-9822(22)00015-X (2022).
21. L. K. Doolittle, M. K. Rosen, S. B. Padrick, Purification of Arp2/3 complex from *Saccharomyces cerevisiae*. *Methods Mol Biol* **1046**, 251–271 (2013).
22. A. Punjani, J. L. Rubinstein, D. J. Fleet, M. A. Brubaker, cryoSPARC: algorithms for rapid unsupervised cryo-EM structure determination. *Nat. Methods* **14**, 290–296 (2017).
23. Y. Z. Tan, *et al.*, Addressing preferred specimen orientation in single-particle cryo-EM through tilting. *Nat. Methods* **14**, 793–796 (2017).

24. R. Sanchez-Garcia, *et al.*, DeepEMhancer: a deep learning solution for cryo-EM volume post-processing. *Commun Biol* **4**, 1–8 (2021).
25. E. F. Pettersen, *et al.*, UCSF Chimera--a visualization system for exploratory research and analysis. *J Comput Chem* **25**, 1605–1612 (2004).
26. R. T. Kidmose, *et al.*, Namdinator - automatic molecular dynamics flexible fitting of structural models into cryo-EM and crystallography experimental maps. *IUCrJ* **6**, 526–531 (2019).
27. P. Emsley, B. Lohkamp, W. G. Scott, K. Cowtan, Features and development of Coot. *Acta Crystallogr. D Biol. Crystallogr.* **66**, 486–501 (2010).
28. P. V. Afonine, *et al.*, Towards automated crystallographic structure refinement with phenix.refine. *Acta Cryst D* **68**, 352–367 (2012).
29. V. B. Chen, *et al.*, MolProbity: all-atom structure validation for macromolecular crystallography. *Acta Crystallogr. D Biol. Crystallogr.* **66**, 12–21 (2010).
30. H. Berman, K. Henrick, H. Nakamura, J. L. Markley, The worldwide Protein Data Bank (wwPDB): ensuring a single, uniform archive of PDB data. *Nucleic Acids Res.* **35**, D301-303 (2007).
31. E. D. Goley, *et al.*, An actin-filament-binding interface on the Arp2/3 complex is critical for nucleation and branch stability. *Proc Natl Acad Sci U S A* **107**, 8159–8164 (2010).
32. A. Zimmet, *et al.*, Cryo-EM structure of NPF-bound human Arp2/3 complex and activation mechanism. *Sci Adv* **6**, eaaz7651 (2020).
33. M. S. Longtine, *et al.*, Additional modules for versatile and economical PCR-based gene deletion and modification in *Saccharomyces cerevisiae*. *Yeast* **14**, 953–961 (1998).
34. A. L. Goldstein, J. H. McCusker, Three new dominant drug resistance cassettes for gene disruption in *Saccharomyces cerevisiae*. *Yeast* **15**, 1541–1553 (1999).
35. M. Rodnick-Smith, Q. Luan, S.-L. Liu, B. J. Nolen, Role and structural mechanism of WASP-triggered conformational changes in branched actin filament nucleation by Arp2/3 complex. *Proc. Natl. Acad. Sci. U.S.A.* **113**, E3834-3843 (2016).
36. J. Schindelin, *et al.*, Fiji: an open-source platform for biological-image analysis. *Nature Methods* **9**, 676–682 (2012).
37. G. M. Hocky, *et al.*, Cations Stiffen Actin Filaments by Adhering a Key Structural Element to Adjacent Subunits. *J. Phys. Chem. B* **120**, 4558–4567 (2016).
38. W. Humphrey, A. Dalke, K. Schulten, VMD: visual molecular dynamics. *J Mol Graph* **14**, 33–38, 27–28 (1996).

39. M. G. Saunders, G. A. Voth, Water Molecules in the Nucleotide Binding Cleft of Actin: Effects on Subunit Conformation and Implications for ATP Hydrolysis. *Journal of Molecular Biology* **413**, 279–291 (2011).
40. J. C. Phillips, *et al.*, Scalable molecular dynamics with NAMD. *Journal of Computational Chemistry* **26**, 1781–1802 (2005).
41. M. J. Abraham, *et al.*, GROMACS: High performance molecular simulations through multi-level parallelism from laptops to supercomputers. *SoftwareX* **1–2**, 19–25 (2015).
42. M. Bonomi, *et al.*, Promoting transparency and reproducibility in enhanced molecular simulations. *Nat Methods* **16**, 670–673 (2019).
43. E. F. Pettersen, *et al.*, UCSF ChimeraX: Structure visualization for researchers, educators, and developers. *Protein Sci* **30**, 70–82 (2021).
44. E. Krissinel, K. Henrick, Inference of macromolecular assemblies from crystalline state. *J. Mol. Biol.* **372**, 774–797 (2007).